14

Phase Diagrams of Carbonate Materials at High Pressures, with Implications for Melting and Carbon Cycling in the Deep Earth

Konstantin Litasov[1,2,3], Anton Shatskiy[1,2,3], Ivan Podborodnikov[1,2,3], and Anton Arefiev[1,2,3]

ABSTRACT

In this chapter, we review phase diagrams of alkali and alkaline earth carbonates at high pressures, particularly simple, binary, and ternary systems, which were recently constrained at pressures of 3 and 6 GPa. These studies revealed a number of new alkali-alkaline earth double carbonates. Major transformations of high-pressure carbonates, including changes in carbon coordination, spin transition, and valence state in Fe-bearing carbonates up to the lower mantle levels, were also discussed. We emphasize the importance of carbonate systems for understanding the low-degree partial melting of carbonated mantle rocks and explaining carbonate inclusions in diamond and other deep-seated minerals. The question of carbonate stability versus the presumably reduced nature of the deep Earth's mantle provides significant impact on the further study of material transport and deep volatile cycle through the history of our planet.

14.1. INTRODUCTION

Carbonates and carbonatite melt can play a key role in the dynamics of the upper mantle and transition zone and may be more important than water or reduced C-O-H compounds (Dasgupta, 2013; Litasov & Shatskiy, 2018). Although total carbon content in the deep Earth is expected to be very low, in the range of hundreds of parts per million, it can be concentrated locally, for example, by the melting of subducted carbonates in the transition zone to produce a significant amount of melt, which can migrate through the mantle towards the lithosphere-asthenosphere boundary. Then, carbonate can segregate below this boundary to form the source region for carbonatite-kimberlite and other alkaline magmas. Even the generation of mid-ocean ridge basalt can be enhanced by carbonate activity at greater depths below ridge axes (Stagno et al., 2013). However, the role of carbonates in the lower mantle is difficult to constrain due to presumably reduced conditions corresponding to iron-wüstite equilibria or even lower fO_2 (Frost & McCammon, 2008) and variable degree of oxidation by subducted slabs penetrating into the lower mantle over time. Overall, carbonates can be involved in all notable mantle processes, including (a) subduction (Dasgupta & Hirschmann, 2010; Plank & Langmuir, 1998; Staudigel, 2014), (b) melting and material transport (Litasov, 2011; Wyllie & Huang, 1976), (c) generation of deep-seated magma (Sharygin et al., 2015; Shatskiy, Litasov, et al., 2017), (d) mantle metasomatism (Agashev et al., 2013; Shu & Brey, 2015; Yaxley & Green, 1996), and (e) diamond formation (Kopylova et al., 2010; Navon et al., 1988).

The origin of carbonates in the deep mantle is difficult to constrain. Subduction of carbonated materials is one of the efficient ways to deliver carbonates as deep as the core-mantle boundary (CMB). However, for Archean-Proterozoic time, the volumes of this delivery could be limited. An important issue is a survival of carbonates in subducted crust and lithosphere through the hydrous melting in the devolatilization region beneath the island

[1] *Sobolev Institute of Geology and Mineralogy, Novosibirsk, Russia*

[2] *Vereshchagin Institute for High Pressure Physics, Moscow, Russia*

[3] *Novosibirsk State University, Novosibirsk,, Russia*

Carbon in Earth's Interior, Geophysical Monograph 249, First Edition. Edited by Craig E. Manning, Jung-Fu Lin, and Wendy L. Mao.

arcs. The existing data indicate almost entire removal of carbonates in the presence of hydrous melt/fluid (Foley et al., 2009; Kelemen & Manning, 2015; Litasov et al., 2011). On the other hand, there are other experimental observations, as well as petrological and numerical modeling data, showing that 20%–80% of subducted carbonates can penetrate beneath the arc devolatilization depths and can be transported to the transition zone or even to the lower mantle (Johnston et al., 2011; Kerrick & Connolly, 2001; Litasov, 2011; Molina & Poli, 2000). Furthermore, the evidences for the deep subduction of carbonates are abundant from the recovered ultra-high-pressure metamorphic rocks worldwide containing diamond and Ca-Mg carbonates (Dobrzhinetskaya et al., 2006).

Carbonates are rare in mantle igneous rocks, xenoliths, and diamonds due to poor solubility of CO_2 in basaltic and alkaline magmas, significant degassing and decarbonation at the subsurface conditions, and postmagmatic alteration. This is particularly applicable for the alkali-bearing carbonates and carbonatites. An example of ultrafast alteration of sodium carbonatites at Oldoinyo Lengai with formation of calcium carbonatites in a matter of days to months (Zaitsev & Keller, 2006) indicates that some of the calcitic and dolomitic carbonatites found in different geological sequences could be initially enriched in Na and K. The scale of carbonate activity in the mantle can be indirectly estimated from the inclusions in diamond and other mantle minerals. Currently, we have various new information about the presence of carbonates in the upper mantle, transition zone, and even the lower mantle. Primary Ca-Mg-carbonates appear in melt pockets in spinel peridotite and eclogite xenoliths (Rudnick et al., 1993; Yaxley et al., 1998) and also in the inclusions in garnet and diamonds (Brenker et al., 2007; Stachel et al., 1998; Zedgenizov et al., 2014).

Recently, various alkali-bearing carbonates were established as inclusions in kimberlite groundmass minerals from Siberia (Golovin et al., 2017). Canada, and Greenland (Kamenetsky et al., 2009, 2013). as well as in minerals from sheared peridotites originated from 180–230 km depths (Golovin et al., 2018; Sharygin et al., 2013). The findings of eitelite- and nyerereite-bearing assemblages in carbonatitic inclusions in diamonds from the Juina (Mato Grosso state, Brazil) (Kaminsky et al., 2016) indicate the possible presence of Na-Ca-Mg carbonatite melts at depths corresponding to the lower mantle. Alkali-bearing fluid and carbonatite melts coexist with peridotite and eclogite minerals in microinclusions in fibrous diamonds, which crystallize prior to the kimberlite eruption (Klein-BenDavid et al., 2009; Logvinova et al., 2011; Navon et al., 1988; Weiss et al., 2009; Zedgenizov et al., 2007, 2011). Similar microinclusions were found along the twinning plane in ancient gem-quality diamonds (Jablon & Navon, 2016). This suggests that alkali-rich carbonate melts have been introduced into the reduced lithospheric mantle since the Archaean and that these melts are responsible for the formation of most diamonds. The important findings of Na-K-Ca-rich carbonatitic inclusions from spinel harzburgites originating from 110–115 km depths indicate that alkali-carbonatite melts can appear in the shallow lithospheric mantle, above the diamond stability field (Giuliani et al., 2012). This is consistent with the interpretation of electrical conductivity anomalies observed in the continental lithospheric mantle 80–120 km beneath the Slave craton (NE Canada) (Jones et al., 2001, 2003) and >120 km beneath the São Francisco craton (SE Brazil) (Pinto et al., 2010) as carbonate-bearing regions based on experimental measurements (Yoshino et al., 2018).

Considering the abundance and importance of carbonates in the shallow Earth's mantle, extensive experimental and theoretical studies have been performed on various carbonate systems at high P-T conditions. The major effect of carbonate on melting of silicate mantle is drastically different from that of hydrous or hydrocarbon fluid and is manifested by the formation of carbonatite magmas, which are stable in equilibrium with peridotite and eclogite in a wide temperature range (Falloon & Green, 1989; Gudfinnsson & Presnall, 2005; Litasov, 2011; Litasov & Shatskiy, 2018; Wyllie & Huang, 1975). Yet Ca-Mg carbonates may be too refractory to initiate melting at geothermal conditions relevant to the continental lithosphere, even in the presence of $FeCO_3$ or H_2O (Irving & Wyllie, 1975; Müller et al., 2017; Shatskiy et al., 2014, 2018). In contrast, minor amounts of alkalis can drastically reduce the solidus temperature of carbonated silicate mantle (Brey et al., 2011; Dasgupta & Hirschmann, 2007a; Grassi & Schmidt, 2011b; Kiseeva et al., 2013; Litasov, 2011; Litasov, Shatskiy, & Ohtani, 2013; Shatskiy, Litasov, & Palyanov, 2015). The decrease in melting temperatures can exceed 400–500 °C relative to alkali-free systems, resulting in a solidus ~100–200 °C below the cratonic geotherm (Litasov, Shatsky, Ohtani, et al., 2013).

Low-degree partial melts in the carbonated peridotite and eclogite systems show strong enrichments in Na_2O and K_2O (Dasgupta & Hirschmann, 2007a; Dasgupta et al., 2004, 2005; Ghosh et al., 2009; Kiseeva et al., 2013; Litasov & Ohtani, 2009, 2010; Sweeney et al., 1995; Wallace & Green, 1988). However, precise determination of the composition of this melt in the natural-like systems with realistic bulk compositions, including very small proportions of CO_2, is problematic due to their trace amounts (Dasgupta & Hirschmann, 2007b; Dasgupta et al., 2004; Sweeney, 1994; Sweeney et al., 1995). In addition, the mass balance calculations for the samples obtained below the apparent solidi often produce clear deficits of alkalis,

suggesting the presence of minor alkali-bearing liquid or solid carbonate phases. In contrast, the study of carbonatite or pure carbonate systems allows careful determination of subsolidus carbonate phases, minimum melting temperatures, and composition of incipient melt, which facilitate interpretation of data obtained in the natural-like carbonate-bearing silicate systems (Litasov, Shatsky, & Ohtani, 2013; Shatskiy, Litasov, & Palyanov, 2015).

Recently, we have thoroughly studied the K-Na-Ca-Mg-Fe carbonate systems at 3–6 GPa (see references in section 14.3) and revealed a number of new alkali-alkaline earth double carbonates (Rashchenko et al., this volume). Here, we review available data on the melting, phase transitions, and phase diagrams of the pure carbonate systems and show their importance for understanding the low-degree partial melting of carbonated mantle rocks. We emphasize the importance of study of pure Na_2CO_3 and K_2CO_3 carbonates for geological purposes, since these endmembers are mandatory for the thermodynamic modeling of alkali-alkaline earth carbonate melts and solids.

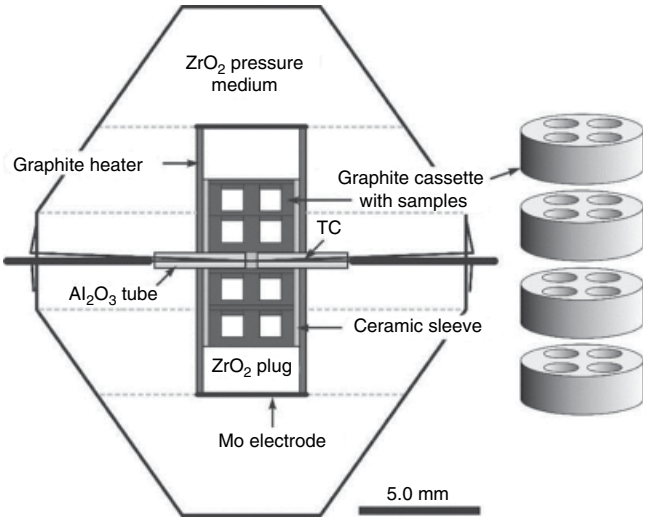

Figure 14.1 High-pressure cell assembly employed to study phase relations in the carbonate systems at 3–6 GPa. The cell contains four graphite cassettes. Each cassette contains four samples. TC – W-$Re_{3\%/25\%}$ thermocouple. See electronic version for color representation of the figures in this book.

14.2. EXPERIMENTAL METHODS

Here we briefly describe several important experimental techniques developed for the study of carbonate and carbonate-silicate systems including particular aspects for sample preparation and electron microprobe measurements. Most experiments were carried out using the DIA-type multianvil apparatuses Discoverer-1500 at the Sobolev Institute of Geology and Mineralogy SB RAS (Novosibirsk, Russia) and similar configuration 3000-ton press at the Department of Earth Sciences (Tohoku University, Sendai, Japan).

Fujilloy N-05 26-mm tungsten carbide cubes with truncation edge length of 12 mm were employed as anvils for Kawai-type cell. Pressure media were made of semi-sintered ZrO_2 ceramics shaped as a 20.5 mm octahedron with ground edges and corners. Pyrophyllite gaskets, 4.0 mm in both width and thickness were used to seal the compressed volume and support the anvil flanks (Shatskiy et al., 2010, 2011). The cell assembly contains four graphite cassettes (multiple sample holders), allowing simultaneous study of 16 samples in a single run (Figure 14.1). The heating was achieved using a tubular graphite heater, 4.5/4.0 mm outer/inner diameter and 11 mm length. The heater and capsules were separated by ceramic sleeve made of talc fired at 1000 °C for 1 hour. The sample temperature was monitored by a $W_{97}Re_3$-$W_{75}Re_{25}$ thermocouple inserted in the heater center via walls and electrically insulated by Al_2O_3 tubes.

The temperature gradients in the cell were examined using thermal modeling software (Hernlund et al., 2006) and verified experimentally (Shatskiy, Sharygin, Gavryushkin et al., 2013) using a two-pyroxene equilibrium (Brey & Kohler, 1990). The maximum temperature gradients within individual sample and across the sample charge were less than 5° and 30 °C/mm at 1300 °C, respectively. We also found no differences in the phase composition of identical samples loaded in different cassettes. The pressure calibration was reported by Shatskiy et al. (2018). Deviation of pressure from the desired value during heating from room temperature in the given cell did not exceed ±0.2 GPa, as confirmed by comparison of pressure calibration at room temperature and 900 °C. In all experiments, no correction for the effect of pressure on the thermocouple electromotive force was applied.

Starting materials were prepared by blending reagent grade Na_2CO_3, K_2CO_3, $CaCO_3$, natural magnesite (<0.1% impurity), dolomite (<0.3% impurity), and siderite (Sd-1: $Fe_{0.95}Mn_{0.05}CO_3$ and Sd-2: $Fe_{0.87}Mn_{0.06}Mg_{0.07}CO_3$) in an agate mortar with acetone and loaded as a powder into graphite cassettes. Since Na_2CO_3 and K_2CO_3 are highly hygroscopic materials, special attention was paid to minimize the amount of moisture in the sample absorbed from the atmosphere. For this purpose, the loaded cassettes were dried at 300 °C for 1–2 h and then prepared assemblies were stored at 200 °C in a vacuum for ≥12 h prior to the experiment. In general, experiments were conducted at low (<25%) indoor humidity.

After completion of the experiments, the recovered graphite cassettes were immediately filled with epoxy in vacuum. Then cassettes were cut using a low-speed diamond saw to get vertical cross-sections of the samples. The obtained specimens were mounted in a Plexiglas holder with epoxy and polished in low-viscosity oil using

a sandpaper. The sample surface was cleaned using an oil spray between each step of polishing. The final polishing was done on a satin cloth with 3 μm diamond paste and oil spray. We used petroleum benzene to remove the oil after polishing. The clean samples were stored in petroleum benzene prior to carbon coating and loading into a scanning electron microscope.

Samples were studied using a MIRA 3 LMU scanning electron microscope (Tescan Orsay Holding) coupled with an INCA-450 energy-dispersive X-ray microanalysis system equipped with the liquid nitrogen-free Large Area EDS X-Max-80 Silicon Drift Detector (Oxford Instruments Nanoanalysis Ltd) at IGM SB RAS (Lavrent'ev et al., 2015). Energy-dispersive X-ray spectra (EDS) were collected by using an electron beam-rastering method, in which the stage is stationary while the electron beam moves over the surface area, with dimensions 5–50 μm (for mineral phases) and 50–500 μm (for a quenched melt) at 20 kV accelerating voltage and 1.5 nA beam current. Live counting time for X-ray spectra was 20–30 s. Sample measurements were always combined with standard carbonate calibrations. This technique allows careful determination of the Na_2O and K_2O contents of carbonates, which can be missing during conventional electron microprobe analyses.

Diamond anvil cell (DAC) experiments on the carbonated systems are usually performed using powdered or single crystal samples with an addition of the internal laser-absorber for sample heating. The typical loading includes carbonate powder mixed with Pt metal and sandwiched between the salt (NaCl, KCl) insulators or pressure medium. Argon or neon gases can also serve as a pressure medium, whereas CO_2 may be placed as a reactant to synthesize carbonates from oxide mixtures. In case of Fe-carbonate, an additional absorber is not needed (Cerantola et al., 2017). The sample is placed between diamond anvils into the hole in the preindented Re gasket. The pressure is calibrated using ruby, metal, neon, or diamond equation of state. The most powerful tool for measurements is an in situ synchrotron X-ray diffraction (Dorfman et al., 2018; Maeda et al., 2017; Martirosyan et al., 2019) with further transmission electron microscopy of recovered sample films. Reliable data can also be obtained by in situ Raman spectroscopy at high temperature or at room temperature on the quenched sample (Bayarjargal et al., 2018). However, DAC has serious limitations related to the achievement of chemical equilibrium, thermal gradient, and temperature measurements in the sample (Dewaele et al., 1998; Kavner & Nugent, 2008; Rainey et al., 2013). Uncertainties in pressure scales of calibrants are essential at pressures above 50–100 GPa. We recommend using recent pressure scales from Sokolova et al. (2013, 2016). where internally consistent equations of state were calculated for most of the important pressure calibrants and can be used for pressure recalculations. In spite of these limitations, the data from DAC experiments are the only available source of information for phase relations at pressures exceeding 30–50 GPa.

The common methods of ab initio computations include density functional theory approach implemented into the VASP or other computer codes using the plane wave basis set and the projector augmented wave method. Exchange-correlation effects have been taken into account in the generalized gradient or local density approximation. Phase diagrams at high temperatures can be calculated using modeling of the Helmholtz free energy within lattice dynamic and the quasi-harmonic approximation or within molecular dynamic simulations. The latter accounts for the effect of anharmonicity at high temperatures more precisely (Gavryushkin et al., 2017; Zhang et al., 2018).

14.3. PHASE DIAGRAMS OF CARBONATES

14.3.1. Melting and Phase Transitions in Simple Carbonate Systems

$CaCO_3$. Recent experimental and theoretical studies indicate that $CaCO_3$ has extremely complex phase diagram at high pressure and many phases are still poorly characterized (Bayarjargal et al., 2018; Gavryushkin et al., 2017; X. Li et al., 2018; Litasov et al., 2017; Lobanov et al., 2017; Ono et al., 2005, 2007; Zhang et al., 2018). The major sequence of phase transitions established from ab initio computations include $R\bar{3}c$ calcite (0–2 GPa), *Pmcn* aragonite (2–42 GPa), *Pmmn* post-aragonite (42–37 GPa), $C222_1$ pyroxene-type structure (137–240 GPa), and *Pmcn*-$CaCO_3$ at higher pressures (Arapan et al., 2007; Oganov et al., 2008). However, near 30 GPa this pattern is complicated by the appearance of several candidate structures with close enthalpies. Their crystal structures vary in different studies. Pickard and Needs (2015) computed the lowest enthalpy for the $P2_1$/c-l phase at 32–48 GPa and $P2_1$c-h for pressures above 67 GPa. Gavryushkin et al. (2017) argued that the most stable phase in the pressure range of 32–46 GPa is $CaCO_3$-VII, which is a polymorph with unit cell parameters of $P2_1$/c-h and atomic arrangement of $P2_1$/c-l. In their study, $P2_1$/c aragonite II and $P2_1$c-l have very close enthalpy to $CaCO_3$-VII. Smith et al. (2018) came to similar conclusions but named $CaCO_3$-VII as $P2_1$c-II. The computation of equation of state from quasi-harmonic approximation and molecular dynamics revealed high-temperature stability of $P2_1$c-l phase and limited stability of $CaCO_3$-VII (Gavryushkin et al., 2017; Smith et al., 2018; Zhang et al., 2018) (Figures 14.2 and 14.3). which is roughly consistent with the experimental data for the pressure range of 25–45 GPa.

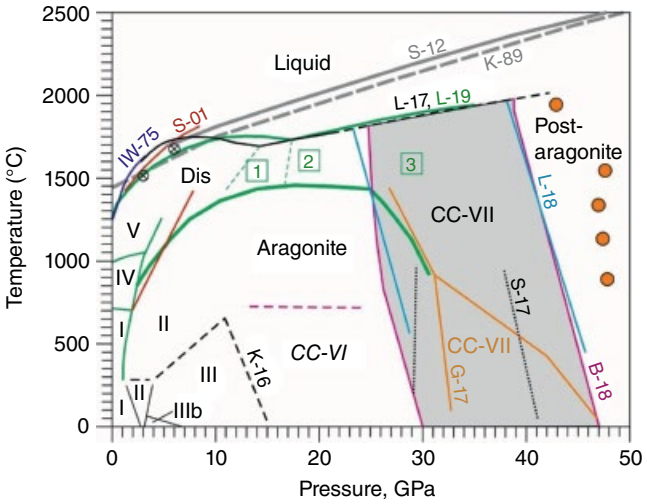

Figure 14.2 Phase diagram of $CaCO_3$ in the pressure range 0–50 GPa. Green lines show melting line and aragonite stability field from present work (L-19). Dis = disordered aragonite. Numbers 1, 2, and 3 indicate observation of new phases. Phase 3 is consistent with $CaCO_3$-VII/$P2_1$/c-l. Other melting lines are from Irving and Wyllie, 1975 (IW-75); Kerley, 1989 (K-89); Suito et al., 2001 (S-01); Spivak et al., 2012 (S-12); and Z. Li et al., 2017 (L-17). Crossed circles show melting points of $CaCO_3$ at 3 and 6 GPa (Shatskiy et al., 2018). Transition boundaries between phases I, II, III, and IIIb are from Pippinger et al. (2015). K-16 = boundary between $CaCO_3$-III and VI (CC-VI) (Koch-Müller et al., 2016). Gray shaded area is the stability field of $CaCO_3$-VII (CC-VII) according to experimental data by X. Li et al., 2018 (L-18), and Bayarjargal et al., 2018 (B-18); and ab initio computations by Gavryushkin et al., 2017 (G-17), and Smith et al., 2018 (S-17). Orange circles indicate observation of CC-VII and post-aragonite in the experiments (Gavryushkin et al., 2017). See electronic version for color representation of the figures in this book.

Experimental observations of the phase transitions in $CaCO_3$ are also highly controversial. At low pressures, calcite transforms to disordered $R\bar{3}m$ modifications IV and V at 715 and 970 °C, respectively (Ishizawa et al., 2013). At low temperatures, several modifications $CaCO_3$-II, III, and IIIb were described. The transition boundaries at 25 °C correspond to the pressures of 1.7 GPa (I → II). 2.0 GPa (II → IIIb). and 3.4 GPa (IIIb → III) (Pippinger et al., 2015). The upper temperature limit of phase II is not well established (Figure 14.2). Phase III transforms to phase VI at about 15 GPa and room temperature (Merlini, Hanfland, et al., 2012). Koch-Müller et al. (2016) observed this transition at higher temperatures with a negative Clapeyron slope (Figure 14.2). The temperature stability of phase VI is poorly resolved (Bayarjargal et al., 2018). The phases II, III, IIIb, and VI were not confirmed by thermodynamic calculations or even clearly observed in the multianvil experiments with better equilibration of the sample at high temperatures. Therefore, these phases can be metastable.

Calcite-aragonite transition was determined in several studies by quench experiments (Irving & Wyllie, 1973), differential thermal analysis (DTA) (Mirwald, 1976), thermodynamic calculations (Salje & Viswanathan, 1976), and electrical impedance measurements (Bagdassarov & Slutskii, 2003). All these data are consistent with later in situ determinations (Suito et al., 2001) and revealed transition at 2 GPa and 700 °C (Figure 14.2). At pressures of 5–8 GPa and 1200–1300 °C, aragonite transforms to a presumably disordered phase observed by the disappearance of most of the diffraction peaks (Figure 14.2). It is not clear whether this phase is similar to $CaCO_3$-V or not. Most likely, it is different from calcite and corresponds to disordered aragonite based on the observation that minor peaks are consistent with aragonite structure. In situ X-ray diffraction in a multianvil apparatus indicates that heating of aragonite at 14 and 19 GPa revealed transition to new phases at temperatures near 1400 °C (Figure 14.2). These phases are not yet characterized. At 29 GPa and 1100 °C, aragonite is transformed to a new phase that has clear similarities with $CaCO_3$-VII. This is in agreement with the data obtained from DAC experiments using both in situ X-ray diffraction (X. Li et al., 2018) and Raman spectroscopy (Bayarjargal et al., 2018). The pressure of the transition is different for 3–4 GPa (Figure 14.2); however, this may be connected with differences in the pressure scales used for the experiments. Bayarjargal et al. (2018) believe that $CaCO_3$-VII and $P2_1$c-l should be the same phase.

Original phase transitions to post-aragonite and to a pyroxene structure were discovered by Ono et al. (2005, 2007). However, phase boundaries were not clearly identified. Phase $P2_1$c-h was synthesized and characterized by Lobanov et al. (2017). Figure 14.3 shows phase boundaries in $CaCO_3$ from ab initio computation (Zhang et al., 2018). These boundaries are consistent with available experimental data except for aragonite to $P2_1$c-l ($CaCO_3$-VII) transition, which was placed at lower pressures.

The melting line of $CaCO_3$ (Figure 14.2) was determined in several works at pressures to 3.5 GPa by quench experiments (Irving & Wyllie, 1975), to about 8 GPa by in situ multianvil experiments (Suito et al., 2001) by electrical conductivity measurements (ECM) and falling sphere method to 21 GPa (Z. Li et al., 2017). DAC experiments at 10–40 GPa (Spivak et al., 2012) and thermodynamic calculations based on properties of calcite, aragonite, and melt (Kerley, 1989). The DAC data are scarce and may overestimate melting temperatures of $CaCO_3$. The results of our new in situ X-ray diffraction multianvil experiments for melting line of $CaCO_3$ obtained at pressures up to 30 GPa with press oscillation procedure are generally in agreement with the results

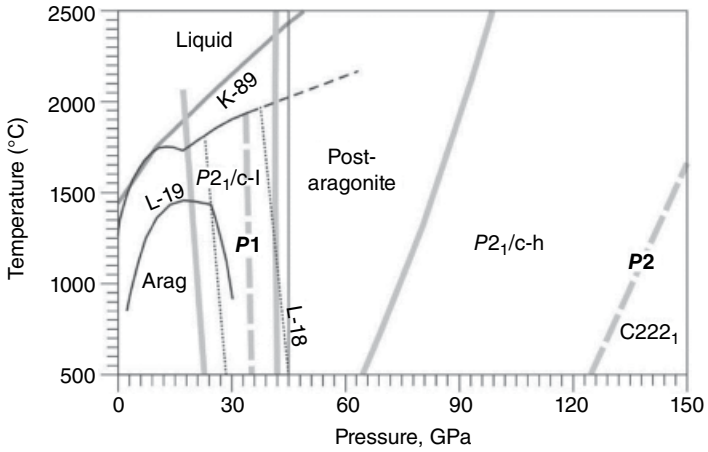

Figure 14.3 Phase transitions in $CaCO_3$ to 150 GPa (Zhang et al., 2018) shown by gray lines. Some data from Figure 14.2 are shown for comparison. P1 and P2 show boundaries of direct transition from aragonite to post-aragonite and to $C222_1$ phase. $P2_1/c$-I is equal to $CaCO_3$-VII. See electronic version for color representation of the figures in this book.

obtained by Z. Li et al. (2017). We may emphasize uncertain position of temperature minimum at solidus connected with phase transition from disordered phase to new high-pressure phase. Z. Li et al. (2017) placed this minimum at 14 GPa, whereas we observed minor minimum near 17 GPa (Figure 14.2).

At temperatures near 3000 °C, which is about 1000 °C above the melting line, $CaCO_3$ melt decomposes to CaO, diamond/graphite and O_2 fluid (Spivak et al., 2012). This temperature is consistent with decomposition parameters revealed by shock compression experiments (Bobrovsky et al., 1976; Ivanov & Deutsch, 2002; Martinez et al., 1995).

$MgCO_3$. Ab initio evolutionary search in the $MgCO_3$ system revealed stability of magnesite at pressures up to 82 GPa, where it transforms to C2/m phase II with three-membered rings of carbonate tetrahedra. Phase II transforms to $P2_1$ phase III with similar structural features. Finally, at ~160 GPa phase III transforms to $Pna2_1$ phase with chains of carbonate tetrahedra (Oganov et al., 2008). In the later study, Pickard and Needs (2015) proposed an additional phase with $P\bar{1}$ symmetry, which was energetically favorable at 85–101 GPa, and $P2_12_12_1$ phase, which was marginally stable along with $P2_1$ structure near 144 GPa. Calculation of high-temperature equations of state indicates limited temperature stability of $P\bar{1}$ phase (<1000 °C) and location of magnesite to phase II transition at 73 GPa with near-zero Clapeyron slope (Zhang et al., 2018). In DAC experiments, transition of magnesite to high-pressure phase was observed at pressures above 100 GPa (Isshiki et al., 2004). In the study of the $MgCO_3$+SiO_2 reaction at lower mantle pressures, magnesite to phase II transition was observed at 76 GPa and 1500 °C (Maeda et al., 2017). which is perfectly consistent with theoretical prediction (Zhang et al., 2018).

Dissociation and melting line of magnesite was determined by quench experiments using piston-cylinder and multianvil technique at pressures to 15 GPa (Byrnes & Wyllie, 1981; Harker & Tuttle, 1955a; Irving & Wyllie, 1975; Katsura & Ito, 1990; Müller et al., 2017; Shatskiy et al., 2018) and in DAC experiments to 84 GPa (Solopova et al., 2015). At pressures below 2.6 GPa, magnesite dissociates to periclase and CO_2 fluid with a narrow pressure range near 3 GPa; it melts incongruently to produce $MgCO_3$–MgO liquid and CO_2 fluid (Figure 14.4). At higher pressures, magnesite melts congruently and its melting line locates slightly above that of $CaCO_3$ (Figure 14.4). The melting line from DAC and large-volume press experiments are consistent with each other. Similar to $CaCO_3$, $MgCO_3$ melt dissociates to MgO, diamond, and O_2 at about 500 °C above the melting line (at 2500–3000 °C) (Solopova et al., 2015).

$FeCO_3$. Phase transitions in $FeCO_3$ were intensively studied using DAC owing to particular interest to spin transitions, valence changes in Fe, and coordination changes in carbon at high pressures (Boulard et al., 2012; Cerantola et al., 2017; Lavina et al., 2009; J. Liu et al., 2015; Lobanov et al., 2015; Mattila et al., 2007). Accordingly, a range of novel carbonate-like phases were discovered upon $FeCO_3$ decomposition at lower mantle pressures. Thermodynamic stability fields of these phases are not yet constrained, just as a detailed ab initio computation on $FeCO_3$ and related compositions has not yet been performed. Figure 14.5 summarizes the schematic phase diagram for $FeCO_3$ (Cerantola et al., 2017). The high-spin to low-spin transition occurs at about 45 GPa (Figure 14.5), whereas two new compounds with tetrahedrally coordinated carbon $R\bar{3}c$ $Fe^{3+}{}_4C_3O_{12}$ and C2/c $Fe^{2+}{}_2Fe^{3+}{}_2C_4O_{13}$ appear at higher pressures of 75–120 GPa and 1000–2200 °C. They coexist with Fe-oxides. Similarly, Fe-oxides and diamond were observed as quench products of siderite decomposition at pressures of 20–60 GPa (Figure 14.5). Mossbauer spectra of the samples quenched from the molten state at temperatures above 1800 °C show unambiguously the presence of $FeCO_3$ as well as iron

oxides: α-Fe_2O_3 (hematite) at pressures below ~25 GPa and HP-Fe_3O_4 (Bykova et al., 2016) at pressures above ~31 GPa. Thus, the location of the melting/dissociation line at pressures above 25 GPa is not clear.

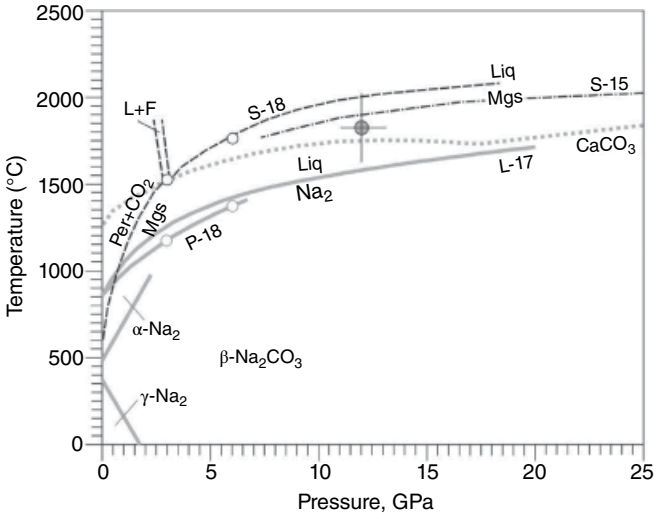

Figure 14.4 Melting and phase transitions in $MgCO_3$ and Na_2CO_3 at pressures to 25 GPa. S-18 = magnesite (Mgs) dissociation and melting line after Shatskiy et al. (2018), including data from Byrnes and Wyllie (1981), Harker and Tuttle (1955a), Irving and Wyllie (1975), and Katsura and Ito (1990). S-15 and grey circle with error bar are results from DAC experiments on magnesite melting (Solopova et al., 2015). Stability of low-pressure Na_2CO_3 phases is after Shatskiy, Litasov, and Palyanov (2015). Melting lines of Na_2CO_3 (Na_2) are after Z. Li et al., 2017 (L-17), and Podborodnikov, Shatskiy, Arefiev, Rashchenko, et al., 2018 (P-18). The $CaCO_3$ melting line (Z. Li et al., 2017) is shown for comparison. See electronic version for color representation of the figures in this book.

The melting line of siderite is not well constrained at lower pressures either. It may strongly depend on the oxidation state during experiment. At pressures below 1 GPa, dissociation lines $FeCO_3 = Fe_3O_4+C+CO_2$ and $Fe_3O_4+C = L+CO_2$ were determined by Weidner (1972, 1982). Tao et al. (2013) performed experiments on dissociation and melting of siderite to 10 GPa and determined the invariant point of transition from dissociation to melting at 7.5 GPa and 1500 °C, whereas Kang et al. (2015) reported the melting line of siderite to 22 GPa. The results of these works do not coincide with our results for decomposition/melting of siderite at 3 and 6 GPa. According to our data, the invariant point should be located near 5.7 GPa and 1570 °C (Figure 14.6). The differences can be explained by peculiarities of experimental technique used, i.e. run duration, details of phase identification, and capsule material, which may affect the oxidation state of the sample. We performed experiments in graphite capsules, which maintain fO_2 near the C–CO_2 (CCO) oxygen buffer and prevent sample oxidation due to large graphite/sample volume ratio. Tao et al. (2013) performed experiments in Pt capsule, which can absorb Fe and cause sample oxidation:

$$4\,FeCO_3\,(\text{siderite}) = Fe^0\,(\text{Fe}-\text{Pt alloy}) + Fe_3O_4\,(\text{magnetite}) + 4\,CO_2\,(\text{fluid}). \quad (14.1)$$

As a result, they observed the $FeCO_3$–Fe_3O_4 eutectics near 1425 °C at 6 GPa, which is 180 °C lower than the siderite melting point established in our experiments. In this case, oxidation state was likely controlled by the FeO–Fe_3O_4 or Fe_3O_4–Fe_2O_3 buffer, which are 1–3 orders of magnitude higher than CCO at 6 GPa and 1400 °C.

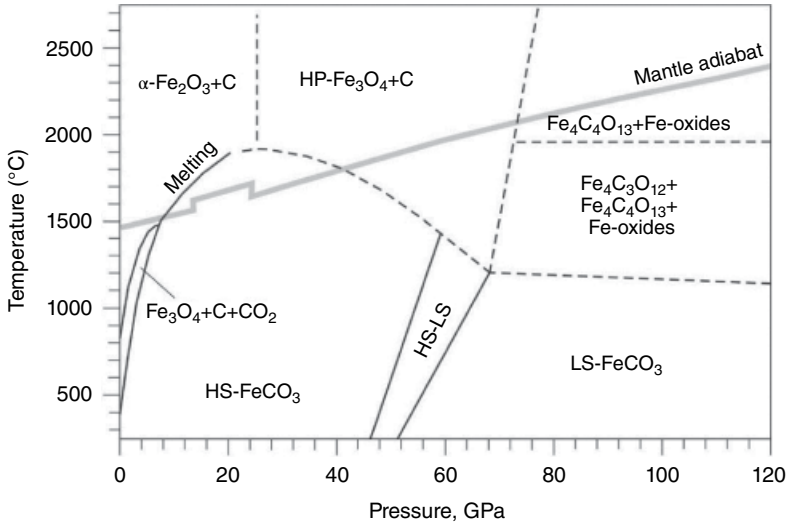

Figure 14.5 Phase transitions in $FeCO_3$ at pressures to 120 GPa (Cerantola et al., 2017). The black solid lines show melting and decomposition of siderite at low pressures (see Figure 14.6) and high-spin to low-spin transition (HS-LS) for magnesiosiderite (J. Liu et al., 2015). The gray line is the mantle adiabat (Litasov & Shatskiy, 2018). See electronic version for color representation of the figures in this book.

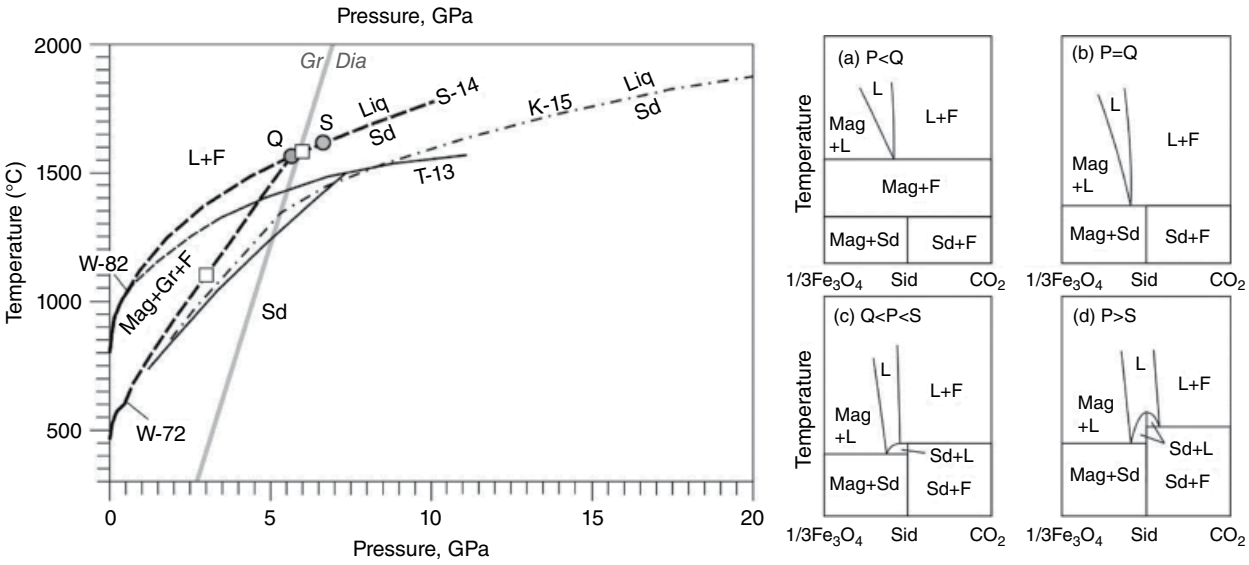

Figure 14.6 The sequence of siderite decomposition reactions, incongruent and congruent melting with increasing pressure based on the experimental data: W-72 = Weidner, 1972; W-82 = Weidner, 1982; T-13 = Tao et al., 2013; S-14 = Shatskiy et al., 2014; K-15 = Kang et al., 2015. Squares show decomposition and melting points of siderite at 3 and 6 GPa. Mag = magnetite; Sd = siderite; Gr = graphite; Q = invariant point, where incongruent melting begins; S = singular point above which congruent melting occurs. Gr/Dia is graphite-to-diamond transition (Kennedy & Kennedy, 1976). Schematic isobaric projections on the right (a–d) illustrate siderite decomposition and melting pathways expected in the Fe–C–3O system. We assume that graphite is present in excess and skip it on these diagrams. See electronic version for color representation of the figures in this book.

Kang et al. (2015) used a double Pt-graphite capsule at 6 GPa and a Au-Pd capsule at 10–20 GPa. The run duration was quite short and did not exceed 1.5 hours at 6 GPa and 20 min at higher pressures. In many subsolidus runs at 10–20 GPa, they observed siderite coexisting with Fe-oxide. This indicates oxidation of the sample and, therefore, lower melting line for siderite. The oxidation can be caused by absorption of Fe by the Au capsule (this may be significant for Fe-rich compositions; Ratajeski & Sisson, 1999) or penetration of oxygen or moisture from cell assembly parts during experiment or from atmosphere prior to loading (this possibility was noticed in the original work). We also suggest oxidation of the sample in Kang et al. (2015) at 6 GPa. Although they used Pt-graphite capsules, their solidus position coincides with that by Tao et al. (2013). In the experiments at 6 GPa we used Sd-2 as starting material, which contains a significant amount of impurities (Shatskiy et al., 2014). At 3 Gpa, we tested both Sd-1 (nearly pure siderite) and Sd-2 and obtained the same results for dissociation point.

Summarizing the data for dissociation and melting of siderite, we can emphasize their dependence on the oxidation state. For the fO_2-conditions close to CCO=0 to CCO–1 (1 log unit below the CCO buffer) at 6 GPa, melting line and invariant point may correspond to our data (Shatskiy et al., 2014); however at more oxidized conditions, when fO_2 is buffered by FeO–Fe_3O_4 (which should be close to quartz–fayalite–magnetite, QFM buffer) the melting line of siderite follows that proposed by Kang et al. (2015) (Figure 14.6).

Na_2CO_3. High-pressure behavior of alkali carbonates is complicated due to the ferroelastic phase transition and lattice melting (Harris & Dove, 1995; Swainson et al., 1995), change of carbon coordination number (CO_3^{2-} to CO_4^{4-}) (Al-Shemali & Boldyrev, 2002; Cancarevic et al., 2007; Mellot-Draznieks et al., 2002), and ability to form disordered (Depater, 1979) and incommensurate (Dusek et al., 2003; Harris & Salje, 1992) phases.

Natrite, γ-Na_2CO_3 (*C*2/*m*), is stable at ambient conditions (Dusek et al., 2003) and transforms to a monoclinic *C*2/*m* β-modification at 330–360 °C, and a hexagonal $P6_3/mmc$ α-phase at 481 °C (Swainson et al., 1995). In situ X-ray diffraction experiments (Shatskiy, Gavryushkin, et al., 2013) revealed the stability of β-Na_2CO_3 at least to 1200 °C at 15.2 GPa (Figure 14.4). Melting curves of Na_2CO_3 obtained by ECM to 18 GPa and falling sphere method at 3 and 6 GPa are marginally consistent with each other and indicate that Na_2CO_3 is the most fusible among major carbonate phases under consideration (Figure 14.4).

Ab initio evolutionary search for stable crystal structures of Na_2CO_3 showed phase transition from γ-Na_2CO_3 to $P6_3/mcm$ phase at 5 GPa and to $P2_1/m$ phase at 35 GPa (Gavryushkin et al., 2016). At the same time, at high pressures orthocarbonate phases with tetrahedrally coordinated carbon can preferentially be stable instead

of carbonates. The phase transition from Na_2CO_3 to Na_4CO_4 (+CO_2) with $I\bar{4}2m$ symmetry was suggested at 40–60 GPa (Cancarevic et al., 2007).

K_2CO_3. Potassium carbonate is monoclinic *C*2/*c* β-K_2CO_3 at ambient conditions (Figure 14.7) and transforms to a hexagonal α-phase (*P*6$_3$/*mmc*) at 420 °C (Becht & Struikmans, 1976; Dinnebier et al., 2005; Schneide & Levin, 1973). The α–β transition was observed using DTA to 0.5 GPa (Klement & Cohen, 1975). The melting temperature of K_2CO_3 was determined by DTA at pressures to 0.5 GPa (Klement & Cohen, 1975); by falling sphere method at 1.8–3.2 GPa (Q. Liu et al., 2007), at 3 and 6 GPa (Arefiev et al., 2018; Shatskiy, Sharygin, Gavryushkin, et al., 2013), and at 4–11.5 GPa; and by ECM to 20 GPa (Z. Li, 2015) (Figure 14.7). The resulting melting lines vary considerably: The differences between three data sets exceeds 250 °C at 6 GPa. This indeed may be connected with the highly hygroscopic nature of K_2CO_3 and possible differences in data obtained by ECM and falling spheres. ECM data indicate a significant positive slope of the K_2CO_3 melting line, which intersects that of $CaCO_3$ at pressures of 10–11 GPa.

In situ X-ray diffraction experiments (Z. Li, 2015) revealed appearance of several new high-pressure modifications of K_2CO_3, which, however, are not characterized and for which phase boundaries are not established (Figure 14.7). There is a definite phase transition at ~4.5 GPa with a solid-solid-liquid triple point bracketed at 1150–1300 °C. This phase transition is either from α to β phase, or from new-1 to new-2.

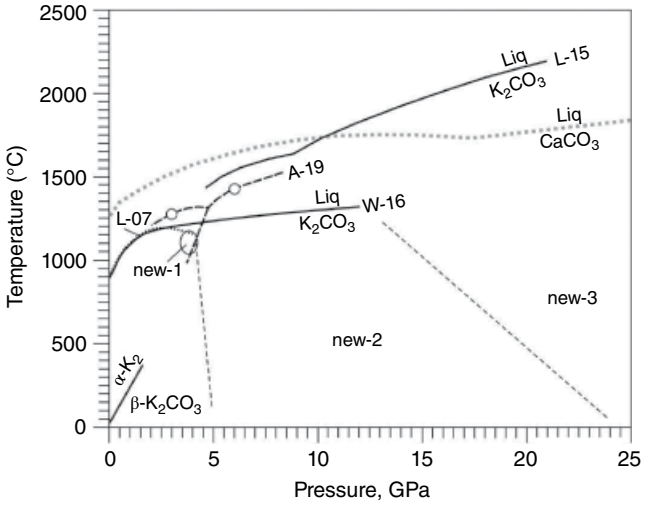

Figure 14.7 Melting lines and phase relations in K_2CO_3. L-07 (dotted curve) = J. Liu et al., 2007; L-15 = Z. Li, 2015; W-16 = Wang et al., 2016; A-19 = Arefiev et al., 2018; Shatskiy, Sharygin, Gavryushkin, et al., 2013b. α-β transition (Klement & Cohen, 1975). New phases 1 (oval field), 2 and 3 and approximate transition lines (Z. Li, 2015). The $CaCO_3$ melting line (Z. Li et al., 2017) is shown for comparison. See electronic version for color representation of the figures in this book.

An ab initio evolutionary search indicates stability of C2/c β-K_2CO_3 (in some works γ-K_2CO_3, as it is isostructural with γ-Na_2CO_3) at pressures to 12 GPa, where it transforms to $P\bar{1}$ structure, which is very similar with $P2_1/m$ Na_2CO_3, and then to *C*2/*c* phase at 53.5 GPa (Gavryushkin et al., 2016). It should be noted that phases predicted by ab initio computations and those observed in in situ X-ray diffraction experiments were not compared with each other. In turn, stability of K_4CO_4 orthocarbonates with $I\bar{4}$ and $P4_2/n$ symmetry was suggested at 25–40 GPa and above 40–45 GPa, respectively (Cancarevic et al., 2007).

14.3.2. Binary Carbonate Systems at High Pressures

Figures 14.8–14.11 summarize data for the binary carbonate systems at pressures of 3 and 6 GPa, which were systematically studied by our group in recent years and compared with low-pressure or 1 atm data. Some of the phases observed in these systems were studied at higher pressures (Golubkova et al., 2015). Crystal structures of the novel high-pressure Na-Ca carbonates are reviewed by Rashchenko et al. (this volume). The studied binary systems include $CaCO_3$-$MgCO_3$ (Shatskiy et al., 2018). Na_2CO_3-$CaCO_3$ at 3 GPa (Podborodnikov, Shatskiy, Arefiev, Rashchenko, et al., 2018) and 6 GPa (Shatskiy, Sharygin, Litasov, et al., 2013). Na_2CO_3–$MgCO_3$ at 3 GPa (Podborodnikov, Shatskiy, Arefiev, Chanyshev, et al., 2018) and 6 GPa (Shatskiy, Gavryushkin, et al., 2013) K_2CO_3–$CaCO_3$ at 3 GPa (Arefiev et al., 2019) and 6 GPa (Shatskiy, Borzdov, et al., 2015). K_2CO_3–$MgCO_3$ at 3 GPa (Arefiev et al., 2018) and 6 GPa (Shatskiy et al., 2013), and Fe-bearing systems at 6 GPa: $FeCO_3$–$MgCO_3$ and K_2CO_3–$FeCO_3$ (Shatskiy, Litasov, Ohtani, et al., 2015). $FeCO_3$–$CaCO_3$ (Shatskiy et al., 2014). and Na_2CO_3–$FeCO_3$ (Shatskiy, Rashchenko, et al., 2015). Previous review of the data available before 2015 with a wider variety of carbonates (such as Li, Ba, Sr-carbonates) was presented by Shatskiy, Litasov, & Palyanov (2015).

$CaCO_3$–$MgCO_3$. This is one of the most important systems in petrology; along with the carbonate-silicate reaction, it determines major features of melting and phase relations in the carbonated systems. Phase relations in the $CaCO_3$–$MgCO_3$ system were studied at $P(CO_2)$ = 0.1 GPa and 625–850 °C (Graf & Goldsmith, 1955), $P(CO_2)$ < 0.1–0.3 GPa and 500–900 °C (Harker & Tuttle, 1955b), $P(CO_2)$ < 1.0 GPa and 700–1200 °C (Goldsmith & Heard, 1961), P = 1.0 GPa and 900–1400 °C (Byrnes & Wyllie, 1981), and P = 3.0 GPa and 1100–1600 °C (Irving & Wyllie, 1975). The studies revealed a two-phase stability field (Mgs + Arg) at low temperatures and limited solid-solutions fields (Mgs + Dol and Dol + Cal/Arg) at higher temperatures (Figure 14.8a, d). The *T*-*X* diagrams have temperature minimums on solidus and liquidus curves that shift from

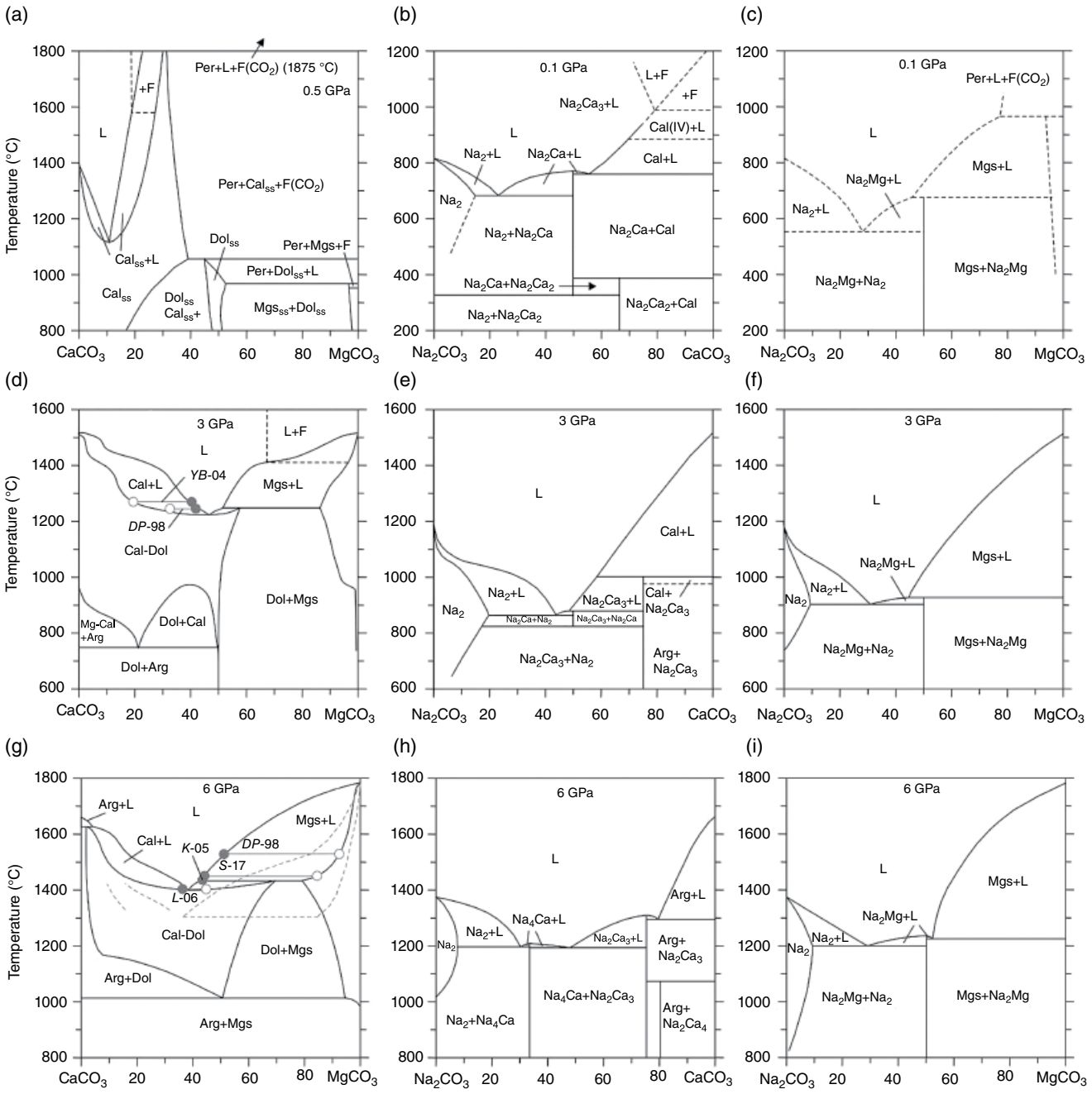

Figure 14.8 Phase relations in binary $CaCO_3$–$MgCO_3$, Na_2CO_3–$CaCO_3$ and Na_2CO_3–$MgCO_3$ systems at 0.1–0.5, 3 and 6 GPa: a = Irving and Wyllie, 1975; b = Cooper et al., 1975. See text for other references. Cal_{SS} = calcite solid solution, Dol_{SS} = dolomite solid solution, Mgs_{SS} = magnesite solid solution, Per = periclase, F = fluid, L = liquid, Na_2 = Na_2CO_3, Na_2Ca = $Na_2Ca(CO_3)_2$, Na_2Ca_2 = $Na_2Ca_2(CO_3)_3$, Cal = calcite, Na_2Mg = $Na_2Mg(CO_3)_2$, Mgs = magnesite, Dol = dolomite, Arg = aragonite, Na_2Ca_3 = $Na_2Ca_3(CO_3)_4$, Na_4Ca = $Na_4Ca(CO_3)_3$, Na_2Ca_4 = $Na_2Ca_4(CO_3)_5$. Black dashed lines = approximate boundaries. Gray dashed lines in (g) = experimental data from Müller et al. (2017). Projected compositions of carbonates (gray open circle) and coexisting melts (gray solid circles) from near solidus experiments in the carbonate-silicate systems: DP-98 = CaO–MgO–Al_2O_3–SiO_2 (CMAS)–CO_2 (Dalton & Presnall, 1998); YB-04 = eclogite (Yaxley & Brey, 2004); K-05 = CMAS–CO_2 (Keshav et al., 2005); L-06 = diopside–CO_2 system (Luth, 2006); S-17 = $CaMgSi_2O_6$+2$MgCO_3$ system (Shatskiy, Podborodnikov, et al., 2017). See electronic version for color representation of the figures in this book.

Ca to Mg side with pressure from Ca# = 58 (Ca# = 100 Ca/(Ca+Mg+Fe) and 1100 °C at 0.5 GPa to Ca# = 58 and 1300 °C at 3 GPa (Figure 14.8a). Our new data at 3 GPa (Shatskiy et al., 2018) indicate that this join is located at slightly lower temperature 1225 °C and Ca# = 53. More significant shift was detected for temperature of the intersection of the Dol-Mgs solvus and the melting loop, which is about 1250 °C in Shatskiy et al. (2018) and 1385 °C in Irving and Wyllie (1975) (Figure 14.8d). The obvious differences are explained by very short duration of the experiments in Irving and Wyllie (1975) and poor identification of chemical compositions in their work. At temperatures above 1425 °C and Ca# ≤ 30, the liquid quenches to dendritic carbonate and periclase and contains rounded voids, indicating an incongruent melting of magnesite to MgO in liquid and CO_2 in fluid and/or liquid (Figure 14.8d).

At 6 GPa the phase diagram was studied by Buob et al. (2006). Müller et al. (2017). and Shatskiy et al. (2018) (Figure 14.8g). Arg + Mgs assemblage is stable below 1000 °C. An appearance of dolomite between 1000 and 1050 °C splits the system into two partial binaries: Arg + Dol and Dol + Mgs. The dolomite-magnesite solvus intersects the melting loop between 1400 and 1450 °C, and forms the isothermal three-phase line, which represents the peritectic reaction: Dol (Ca# 31) = Mgs (Ca# 21) + liquid (Ca# 57). The melting loop for the $CaCO_3$–$MgCO_3$ join has a liquidus minimum at 1400 °C and Ca# = 62. The robustness of the obtained data for the $CaCO_3$–$MgCO_3$ system is confirmed by the excellent consistency of the geometry of the $CaCO_3$–$MgCO_3$ melting loop at 3 and 6 GPa with phase relations in the carbonated eclogite (Yaxley & Brey, 2004) and peridotite (Dalton & Presnall, 1998) systems, where Ca-dolomite melt coexists with Mg-calcite in eclogite and peridotite at 3 GPa, and dolomite melt coexists with magnesite in peridotite at 6 GPa (Figure 14.8d, g). In Müller et al. (2017). the liquidus minimum and dolomite-magnesite solvus are located at 100–150 °C lower, relative to the data by Shatskiy et al. (2018) (Figure 14.8g). It is difficult to explain these uncertainties. They may be related to a limited amount of experiments in Müller et al. (2017), calibration of the temperature measurements, and unavoidable hydration of the sample by, for example, parts of the cell assembly.

The $CaCO_3$–$MgCO_3$ system contains the important intermediate compound dolomite, which was intensively studied at high pressures. Original experiments on dolomite stability showed its decomposition to magnesite and aragonite at pressures near 5–6 GPa (Figure 14.9). There are some uncertainties between the data in different works; however, major consistency is observed near 6 GPa and 1000 °C (Hermann et al., 2016; Luth, 2001; Martinez et al., 1996; Morlidge et al., 2006; Shirasaka et al., 2002; Tao et al., 2014). Later dolomite composition

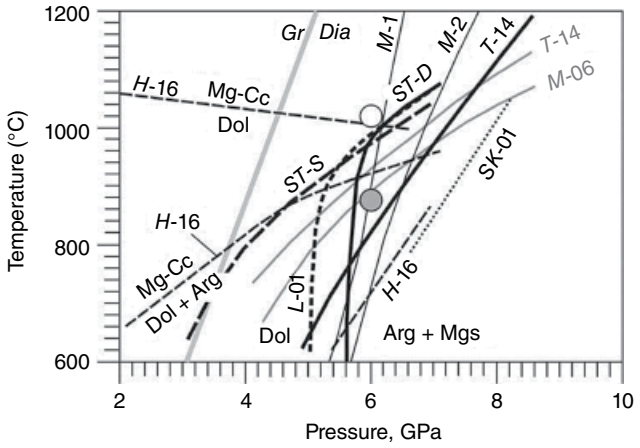

Figure 14.9 Decomposition boundary of $CaMg(CO_3)_2$ dolomite (black lines) and $CaFe(CO_3)_2$ ankerite solid solution (gray lines). SK-01 = Sato & Katsura, 2001; L-01 = (Luth, 2001); ST-D = dolomite decomposition, and ST-S = dolomite synthesis experiments (Shirasaka et al., 2002); M-1 and M-2 = thermodynamic estimations of phase transition (Martinez et al., 1996); T-14 = Tao et al., 2014; M-06 = Morlidge et al., 2006. The reactions from Hermann et al. (2016) (H-16) correspond to Dol = Mg-Cc (Mg-rich Ca-carbonate); Dol+Arg = Mg-Cc and Dol = Arg+Mgs. Open circle = our data for dolomite at 6 GPa (Shatskiy et al., 2018). Gray circle = our data for ankerite solid solution at 6 GPa (Shatskiy et al., 2014). Thick gray line is graphite to diamond transition (Kennedy & Kennedy, 1976). See electronic version for color representation of the figures in this book.

was reinvestigated at very high pressures, where it can reappear as a stable phase with different crystal structures if one adds >10 mol.% $FeCO_3$ to dolomite (see section 14.3.3). In pure $CaMg(CO_3)_2$ composition, dolomite transforms to high-pressure dolomite-II with $CaCO_3$-III-like structure upon compression to 20 GPa (Santillán et al., 2003). Merlini et al. (2017) showed that dolomite II transforms further to dolomite IIIc with $P\bar{1}$ symmetry (Z = 8). This crystal structure is different from Fe-dolomite III and IIIb (see below). Stability of high-pressure polymorphs of dolomite upon heating is not reported.

Na_2CO_3–$CaCO_3$. The phase relations in the Na_2CO_3–$CaCO_3$ reveal several intermediate compounds, which are different at 0.1, 3, and 6 GPa (Figure 14.8). At 0.1 GPa, the system has one intermediate phase, nyerereite $Na_2Ca(CO_3)_2$, near the solidus at 400–700 °C. It melts congruently at 817 °C and 0.1 GPa. $Na_2Ca(CO_3)_2$ is unstable below 300 °C and breaks down into calcite and shortite $Na_2Ca_2(CO_3)_3$ (Cooper et al., 1975) (Figure 14.8b). At 3 GPa, the system has two intermediate compounds, $Na_2Ca(CO_3)_2$ and $Na_2Ca_3(CO_3)_4$, at 850 °C. The maximum solubility of $CaCO_3$ in Na_2CO_3 is 20 mol.% at 850 °C. The Na_2CO_3–$Na_2Ca(CO_3)_2$ eutectic locates near 860 °C and 56 mol.% Na_2CO_3. $Na_2Ca(CO_3)_2$ melts incongruently to $Na_2Ca_3(CO_3)_4$ and a liquid containing about 51 mol.% Na_2CO_3 at ~880 °C.

$Na_2Ca_3(CO_3)_4$ disappears above 1000 °C via incongruent melting to calcite and a liquid containing about 43 mol.% Na_2CO_3 (Figure 14.8e) (Podborodnikov, Shatskiy, Arefiev, Rashchenko, et al., 2018).

At 6 GPa, the system has three eutectics at 1200 °C and 70 mol.% Na_2CO_3, at 1200 °C and 52 mol.% Na_2CO_3, and at 1300 °C and 21 mol.% Na_2CO_3, and three intermediate compounds. Two of them, $Na_4Ca(CO_3)_3$ and $Na_2Ca_3(CO_3)_4$, melt congruently at 1210 and 1310 °C, respectively, and one, $Na_2Ca_4(CO_3)_5$, decomposes to the $Na_2Ca_3(CO_3)_4$ + aragonite at 1100 °C (Figure 14.8h) (Shatskiy, Sharygin, Litasov, et al., 2013; Shatskiy, Rashchenko, et al., 2015). The maximum solubility of $CaCO_3$ in Na_2CO_3 is 6–8 mol.% at 1100–1300 °C, whereas Na_2CO_3 solubility in aragonite does not exceed the detection limit (<0.5 mol.%). Thus, a range of the intermediate compounds along the $CaCO_3$–Na_2CO_3 join changes with increasing pressure in the following sequence: $Na_2Ca(CO_3)_2$, $Na_2Ca_2(CO_3)_3$ (0.1 GPa) → $Na_2Ca(CO_3)_2$, $Na_2Ca_3(CO_3)_4$ (3 GPa) → $Na_4Ca(CO_3)_3$, $Na_2Ca_3(CO_3)_4$, $Na_2Ca_4(CO_3)_5$ (6 GPa). Thus, the nyerereite stability field extends to the shallow mantle pressures, whereas the shortite stability field terminates somewhere between 0.1 and 3 GPa. Consequently, findings of nyerereite and shortite among daughter phases in the melt inclusions in olivine from the sheared garnet peridotites are consistent with their mantle origin.

Na_2CO_3–$MgCO_3$. Phase relations in the system Na_2CO_3–$MgCO_3$ at ambient or low pressures have not been studied so far. Schematic diagram is presented in Figure 14.8c. The system has likely one intermediate compound, $Na_2Mg(CO_3)_2$ eitelite. It was constrained using available data on eitelite melting at 0.12 GPa and 677 °C (Eitel & Skaliks, 1929) and eitelite stability in the related systems $K_2Ca(CO_3)_2$–$Na_2Mg(CO_3)_2$ (McKie, 1990) and Na_2CO_3–MgF_2 at 0.1 GPa (Mitchell & Kjarsgaard, 2011). Eitelite is stable in the subsolidus assemblages below 550 °C in both systems.

At 3 and 6 GPa, the subsolidus system topology is not changed (Figure 14.8f, i). The subsolidus assemblages comprise two fields of Na_2CO_3 + eitelite and eitelite + magnesite. At 3 GPa, the Na-carbonate–eitelite eutectic was established at 900 °C and 69 mol.% Na_2CO_3. Eitelite melts incongruently to magnesite and a liquid containing about 55 mol.% Na_2CO_3 at 925 ± 25 °C. At 6 GPa, the system has two eutectics at 1200 °C and 71 mol.% Na_2CO_3 and at 1250 °C and 48 mol.% Na_2CO_3. Eitelite melts congruently at 1225 °C. The $MgCO_3$ solubility in Na_2CO_3 approaches 9 mol.% at 900 °C and 3 GPa and 10 mol.% at 1200 °C and 6 GPa, whereas Na_2CO_3 contents in $MgCO_3$ are below detection limit (Podborodnikov, Shatskiy, Arefiev, Chanyshev et al., 2018; Shatskiy, Gavryushkin, et al., 2013).

Compression of $Na_2Mg(CO_3)_2$ at room temperature reveals a phase transition to high-pressure phase at 14 GPa; however, its crystal structure is not yet characterized (Golubkova et al., 2015).

K_2CO_3–$CaCO_3$. The system K_2CO_3–$CaCO_3$ was studied at ambient pressure within 50–100 mol.% K_2CO_3 (Niggli, 1916) and 0–50 mol.% K_2CO_3 (Kröger et al., 1943). Similar to ambient pressures at 0.1 GPa, the system has two intermediate compounds near the solidus at 600–700 °C $K_2Ca(CO_3)_2$ (fairchildite) and $K_2Ca_2(CO_3)_3$ (Figure 14.10a) (Cooper et al., 1975). Below 512 °C, $K_2Ca_2(CO_3)_3$ becomes unstable and breaks down into calcite and $K_2Ca(CO_3)_2$ (buetschlite). Fairchildite melts congruently at 809 °C, whereas $K_2Ca_2(CO_3)_3$ melts incongruently to calcite + liquid at 810 °C. Mutual solubility of the endmembers was not well studied. It was suggested that $CaCO_3$ solubility in K_2CO_3 is up to 18 mol.%.

At 3 GPa and 800 °C (Figure 14.10b). the system has also two intermediate compounds: $K_2Ca(CO_3)_2$ buetschliite, and $K_2Ca_2(CO_3)_3$. However, at 850 °C, a third compound, $K_2Ca_3(CO_3)_4$, appears. The K-carbonate–$K_2Ca(CO_3)_2$ eutectic is established near 970 °C and 56 mol.% K_2CO_3. $K_2Ca(CO_3)_2$ melts incongruently at 990 °C to $K_2Ca_2(CO_3)_3$ and a liquid containing 53 mol.% K_2CO_3. In turn, $K_2Ca_2(CO_3)_3$ melts congruently just above 1100 °C. The $K_2Ca_2(CO_3)_3$–$K_2Ca_3(CO_3)_4$ eutectic locates near 1085 °C and 29 mol.% K_2CO_3. $K_2Ca_3(CO_3)_4$ melts incongruently at 1100 °C to calcite and a liquid containing 28 mol.% K_2CO_3. The maximum solubility of $CaCO_3$ in K_2CO_3 is 18 mol.% at 950 °C (Arefiev et al., 2019).

At 6 GPa, the system has three eutectics at 1180 °C and 63 mol.% K_2CO_3, at 1180 °C and 44 mol.% K_2CO_3, and at 1300 °C and 23 mol.% K_2CO_3, as well as three intermediate compounds. Two intermediate phases, $K_8Ca_3(CO_3)_7$ and $K_2Ca_3(CO_3)_4$, melt congruently at 1225 °C and 1350 °C, respectively (Figure 14.10c). The $K_2Ca(CO_3)_2$ compound decomposes to $K_8Ca_3(CO_3)_7$ + $K_2Ca_3(CO_3)_4$ above 950 °C. $CaCO_3$ solubility in K_2CO_3 and K_2CO_3 solubility in aragonite are below the detection limit (<0.5 mol.%) (Shatskiy, Borzdov, et al., 2015). This indicates significant differences in crystal structure of K_2CO_3 at 3 and 6 GPa, which is consistent with the phase transition near 4.5 GPa (Figure 14.7).

The crystal structures of different K-Ca phases obtained at 3–6 GPa have not been determined yet. Preliminary single crystal X-ray diffraction data for $K_2Ca_3(CO_3)_4$ show an existence of two quenchable polymorphs at 3 and 6 GPa. Both phases are orthorhombic and have very similar unit cell parameters: a = 7.38749(17) Å, b = 8.8128(2) Å, c = 16.4873(4) Å for the 3 GPa polymorph with space group $P2_12_12_1$; and a = 7.53915(18) Å, b = 8.7799(2) Å, c = 16.1811(4) Å for the 6 GPa polymorph with space group *Pnam*. Higher symmetry of the 6 GPa polymorph together with broadening of its Raman bands suggests that it may be a disordered variety of the ordered 3 GPa counterpart (Arefiev et al., 2019).

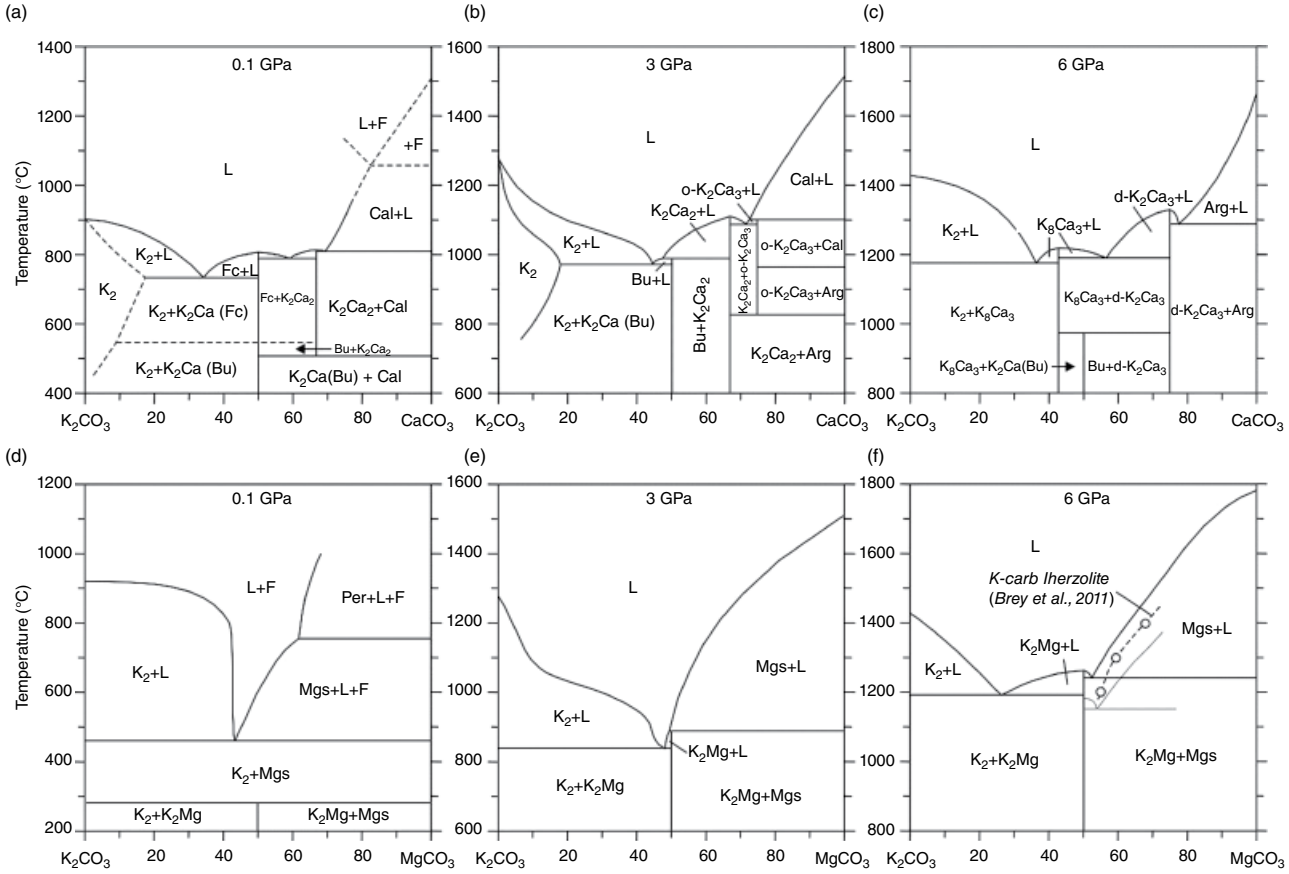

Figure 14.10 Phase relations in binary K_2CO_3–$CaCO_3$ and K_2CO_3–$MgCO_3$ systems at 0.1, 3, and 6 GPa: a = Cooper et al., 1975; d = Ragone et al., 1966. See text for other references. K_2 = K_2CO_3, K_2Ca = $K_2Ca(CO_3)_2$, Bu = buetschliite, Fc = fairchildite, K_2Ca_2 = $K_2Ca_2(CO_3)_3$, Cal = calcite, F = fluid, L = liquid, o-K_2Ca_3 = ordered $K_2Ca_3(CO_3)_4$, Arg = aragonite, K_8Ca_3 = $K_8Ca_3(CO_3)_7$, d-K_2Ca_3 = disordered $K_2Ca_3(CO_3)_4$, Per = periclase, K_2Mg = $K_2Mg(CO_3)_2$, Mgs = magnesite. Dashed lines = approximate boundaries. Melt compositions from K-bearing carbonated peridotite (Brey et al., 2011) is shown at f along with part of K_2CO_3–$FeCO_3$ diagram (gray lines) (see Figure 14.11d). See electronic version for color representation of the figures in this book.

Thus, a range of K-Ca double carbonates changes upon pressure and temperature increase in the following sequence: $K_2Ca(CO_3)_2$ (buetschliite), $K_2Ca_2(CO_3)_3$ (≤0.1 GPa; < 547 °C) → $K_2Ca(CO_3)_2$ (fairchildite), $K_2Ca_2(CO_3)_3$ (≤0.1 GPa; 547–835 °C) → $K_2Ca(CO_3)_2$ (buetschliite), $K_2Ca_2(CO_3)_3$, $K_2Ca_3(CO_3)_4$ (ordered) (3 GPa; 800–1100 °C) → $K_8Ca_3(CO_3)_7$, $K_2Ca(CO_3)_2$ (buetschliite), $K_2Ca_3(CO_3)_4$ (disordered) (6 GPa; 900–1300 °C) (Arefiev et al., 2019).

K_2CO_3–$MgCO_3$. The system K_2CO_3–$MgCO_3$ at $P(CO_2)$ = 3.4 MPa (Eitel & Skaliks, 1929) and at 0.1 GPa (Figure 14.10d) (Ragone et al., 1966) contains one intermediate phase $K_2Mg(CO_3)_2$ below 300 °C. It has an *R3m* space group at 25 MPa (Hesse & Simons, 1982) and breaks down into K_2CO_3 and $MgCO_3$ at higher temperatures. The eutectic is located at 460 °C and 56 mol.% K_2CO_3. Magnesite melts incongruently at 755 °C to periclase + liquid containing 37 mol.% K_2CO_3.

At 3 GPa, two fields appear at subsolidus conditions: K_2CO_3 + $K_2Mg(CO_3)_2$ and $K_2Mg(CO_3)_2$ + $MgCO_3$ with the boundary near 50 mol.% K_2CO_3. The K_2CO_3–$K_2Mg(CO_3)_2$ eutectic is located at 840 °C and 52 mol.% K_2CO_3. $K_2Mg(CO_3)_2$ melts incongruently at 890 °C to magnesite and a liquid containing 51 mol.% K_2CO_3. (Figure 14.10e) (Arefiev et al., 2018). At 6 GPa, the system has two eutectics at 1200 °C and 75 mol.% K_2CO_3 and at 1300 °C and 48 mol.% K_2CO_3, and the same stable intermediate phase, $K_2Mg(CO_3)_2$, which melts congruently near 1250 °C (Shatskiy, Sharygin, Gavryushkin, et al., 2013).

The near-solidus melt of K-bearing carbonated peridotite at 6 GPa and 1200 °C is dominated by K_2CO_3 (40.8 mol.%) and $MgCO_3$ (45.5 mol.%). It also contains 6.0 mol.% $FeCO_3$ and 5.5 mol.% $CaCO_3$. With increasing temperature from 1200 to 1400 °C, the melt evolves towards Mg-Fe-rich compositions. The SiO_2 content of the melt in this temperature range increases from 1.1 to 4.8 mol.% (Brey et al., 2011). The compositions of partial melts are broadly consistent with those in the K_2CO_3–$MgCO_3$ (Figure 14.10f) and K_2CO_3–$FeCO_3$ binaries (Figure 14.11d). Consequently, the partial melt composition in K-rich carbonated lherzolite at 6 GPa and 1200–1400 °C is determined by melting phase relations along the K_2CO_3–(Mg,Fe)CO_3 join. Golubkova et al. (2015) reported a phase transition of $K_2Mg(CO_3)_2$ to monoclinic phase upon compression to 8.1 GPa.

$FeCO_3$–$MgCO_3$. Similar to the $FeCO_3$ phase diagram, there are some uncertainties in phase relations in the binary $FeCO_3$–$MgCO_3$ systems at 3–6 GPa. At 3 GPa, we observed dissociation of siderite at 1100 °C. Accordingly, we constrained an approximate phase diagram (Figure 14.11a). At 6 GPa, a continuous solid solution phase diagram was established with experimental points up to 1700 °C (Shatskiy, Litasov, Ohtani, et al., 2015b). Alternative phase diagrams with asymmetric melting loop were proposed by Kang et al. (2016). They constrained thermodynamic model and calculated phase diagrams in the Fe-rich part of the system with liquidus and solidus minimum located at 10 GPa, 18 mol.% $MgCO_3$, and 1580 °C; and at 20 GPa, 28 mol.% $MgCO_3$, and 1830 °C. At present, this model is too speculative and is not sufficiently supported by experimental data; therefore, we only mention it here.

$FeCO_3$–$CaCO_3$. Subsolidus phase relations in the system $FeCO_3$–$CaCO_3$ were investigated at $P(CO_2)$ = 0.2–0.4 GPa and 300–550 °C (Rosenberg, 1963), 1.5 GPa and 600–800 °C (Goldsmith et al., 1962), 2–3 GPa and 650–800 °C (Davidson, 1994), and at 3.5 GPa and 600–900 °C (Franzolin et al., 2011). The experiments show a large miscibility gap of calcium and iron carbonates at low temperatures, which narrows with increasing temperature and terminates near 1000 °C. Pressure does not affect the topology of diagrams within the studied range. Piston-cylinder experiments in double Pt-graphite capsules (Franzolin et al., 2011) resulted in decomposition of $Fe_{0.75}Ca_{0.25}CO_3$ in the Fe-rich part of the system at 1100 °C and 3.5 GPa:

$$12\,Fe_{0.75}Ca_{0.25}CO_3 = 6\,Fe_{0.5}Ca_{0.5}CO_3 + 2\,Fe_3O_4 + C + 5\,CO_2. \quad (14.2)$$

At 6 GPa, the $FeCO_3$–$CaCO_3$ system shows melting loop with a minimum on the liquidus/solidus curves established at 1280 °C and 56 mol.% $CaCO_3$ (Figure 14.10b) (Shatskiy et al., 2014). At low temperatures, the existence of solid solutions is limited by the appearance of siderite + ankerite assemblage at about 900 °C and ankerite + aragonite below 1000 °C. Below 880 °C, ankerite is unstable and decomposes into siderite and aragonite (Figure 14.9) (Morlidge et al., 2006; Tao et al., 2014). Aragonite solid solution can be transformed to disordered phase at temperatures above 1200 °C (Figure 14.2). The formation of CO_2 fluid and presence of iron oxide among quenched products of carbonate melt within 0–30 mol.% $CaCO_3$ and 1500–1700 °C indicate incongruent dissolution of siderite in the melt above 1500 °C.

Na_2CO_3–$FeCO_3$. At 6 GPa, the system Na_2CO_3–$FeCO_3$ has eutectic at 1000 °C and 66 mol.% Na_2CO_3 and one intermediate compound $Na_2Fe(CO_3)_2$, which melts incongruently at 1050 °C to siderite and melt with 55 mol.% Na_2CO_3 (Figure 14.11c) (Shatskiy, Rashchenko, et al., 2015).

K_2CO_3–$FeCO_3$. At 6 GPa, the system K_2CO_3–$FeCO_3$ has two eutectics at 1200 °C and 74 mol.% K_2CO_3 and at 1250 °C and 48 mol.% K_2CO_3, and one intermediate compound $K_2Fe(CO_3)_2$, which melts congruently at 1210 °C (Figure 14.11d) (Shatskiy, Litasov, Ohtani, et al., 2015).

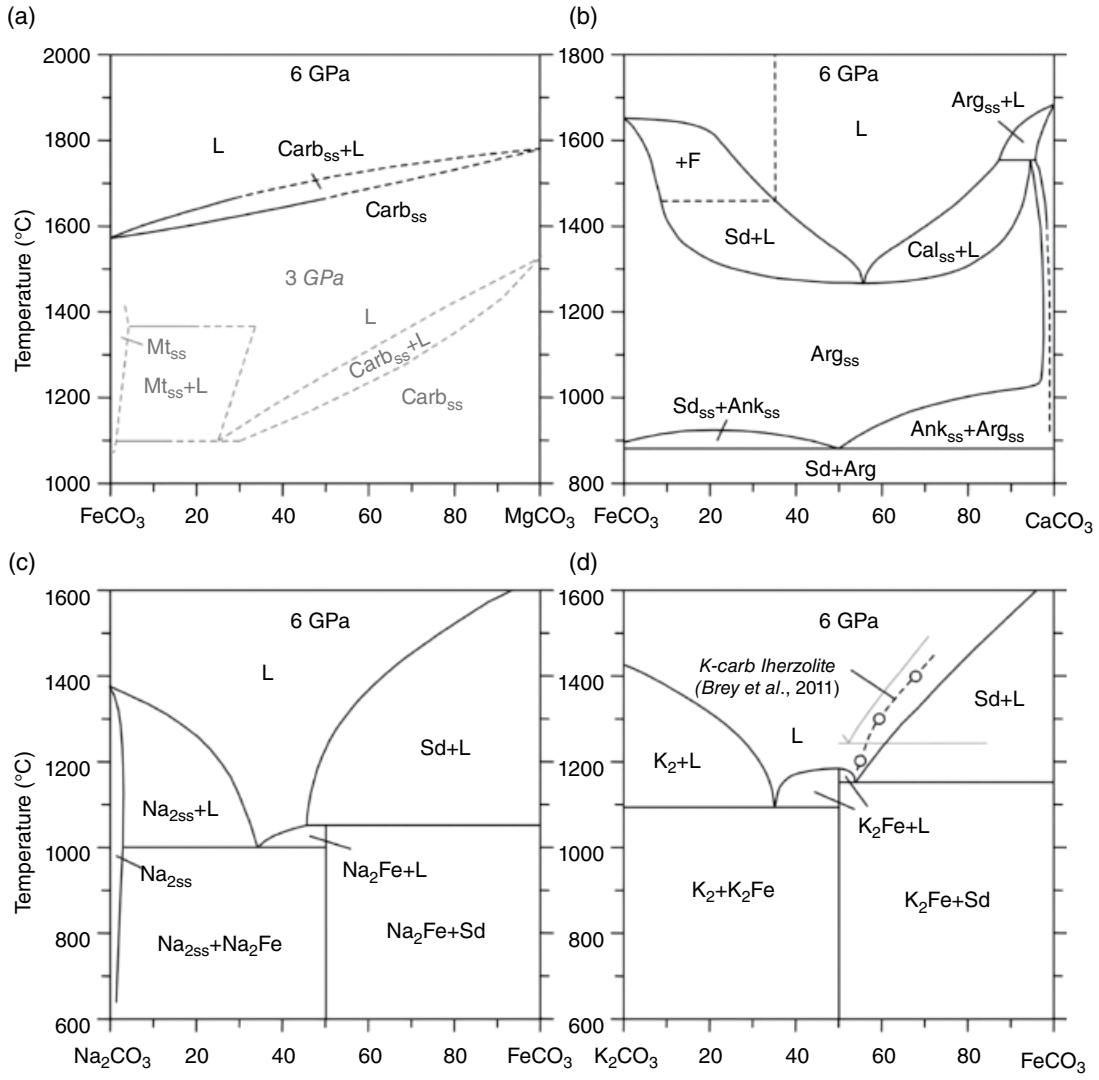

Figure 14.11 Phase relations in the binary siderite-bearing systems at 6 GPa (Shatskiy et al., 2014; Shatskiy, Litasov, Ohtani, et al., 2015; Shatskiy, Rashchenko, et al., 2015). Mt_{ss} = magnetite solid solution, $Carb_{ss}$ = Mg-Fe carbonate solid solution, L = liquid, F = fluid, Sd_{ss} = siderite solid solution, Ank_{ss} = ankerite solid solution, Arg_{ss} = aragonite solid solution, Cal_{ss} = calcite solid solution, Na_{2ss} = Na-carbonate solid solution, Na_2Fe = $Na_2Fe(CO_3)_2$, Sd = siderite, K_2 = K_2CO_3, K_2Fe = $K_2Fe(CO_3)_2$. Dashed lines = estimated boundaries. Gray lines at (a) show phase diagram at 3 GPa (our data in preparation). Melt compositions from K-bearing carbonated peridotite (Brey et al., 2011) is shown at (d) along with part of K_2CO_3–$MgCO_3$ diagram (gray lines) (see Figure 14.10f). See electronic version for color representation of the figures in this book.

14.3.3. Ternary Carbonate Phase Diagrams

$CaCO_3$–$FeCO_3$–$MgCO_3$. Subsolidus phase relations in the ternary system $CaCO_3$–$MgCO_3$–$FeCO_3$ were studied under the same conditions as $CaCO_3$–$FeCO_3$ system (see references in previous section). The resulting diagrams show limited solid solutions of $FeCO_3$ in $CaCO_3$ and a complete series of $FeCO_3$ and $MgCO_3$ solid solutions at 3.5 GPa (Figure 14.12) (Franzolin et al., 2011). The solubility of siderite in calcite and calcite in ankerite increases with temperature. At 6 GPa, incorporation of $FeCO_3$ extends the zone of dolomite–ankerite solid solutions into the low-temperature portion of phase diagram (Shatskiy et al., 2014). At the same time, obtained data suggest a minor decrease in the minimum melting temperature with adding geologically relevant amounts of siderite or ankerite in the $MgCO_3$–$CaCO_3$ system, because the minimum melting temperature of the $FeCO_3$–$CaCO_3$ system is less than 100 °C lower than that of $MgCO_3$–$CaCO_3$ (Figure 14.12). Indeed, no melting

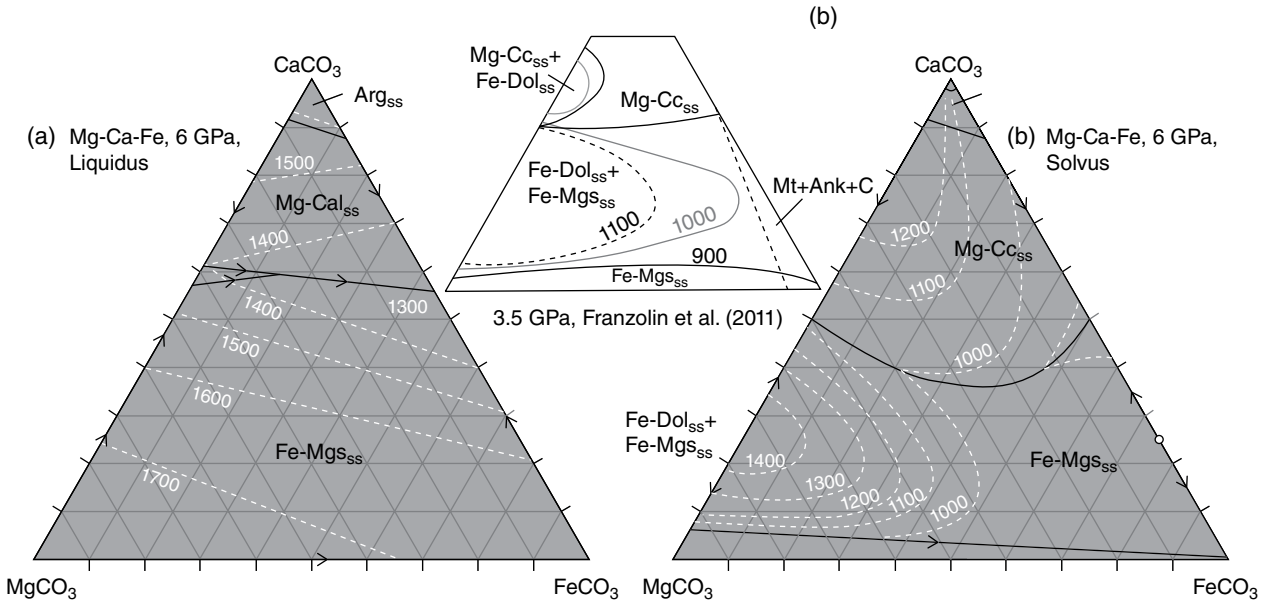

Figure 14.12 Phase relations in the system $CaCO_3$–$FeCO_3$–$MgCO_3$ at 6 GPa (Shatskiy et al., 2014). Inset shows solvus projections at 3.5 GPa and 900–1100 °C (Franzolin et al., 2011). Arg = aragonite; Mg-Cal = Mg-calcite; Mg-Cc = Mg-Ca-carbonate; Fe-Mgs = Fe-Mg carbonate; Fe-Dol = Fe-dolomite; SS = solid solution; Mt = magnetite; Ank = ankerite. See electronic version for color representation of the figures in this book.

occurs along the $FeCO_3$–$Ca_{0.5}Mg_{0.5}CO_3$ join at 1300 °C and 6 GPa.

An addition of Fe-carbonate to dolomite stabilizes this compound at pressures exceeding 20 GPa. Two compositions have been studied. Mao et al. (2011) investigated phase transitions in natural $Ca_{0.99}Mg_{0.92}Fe_{0.08}Mn_{0.01}(CO_3)_2$ dolomite. They observed transition to dolomite II at 17 GPa. Laser heating of the sample in DAC at 27–30 GPa revealed stability of dolomite II to 1400 °C and decomposition to $CaCO_3$ and magnesite at a higher temperature. Heating of the sample at 36–40 GPa indicates appearance of new phase dolomite III, which was stable near 1250 °C.

Merlini, Crichton, et al. (2012) refined crystal structures of phases synthesized from $Ca(Mg_{0.6}Fe_{0.4})(CO_3)_2$ composition using DAC. Dolomite II appears at 17 GPa and crystallizes in triclinic $P\bar{1}$ symmetry with Z = 4. Dolomite III appears at 36 GPa and has the same $P\bar{1}$ space group with Z = 8, but with significantly different structure. Laser heating indicates stability of dolomite III to 2300 °C at 43 GPa, i.e. to temperatures close to the melting point. X-ray diffraction of dolomite III is not consistent with that of dolomite III from Mao et al. (2011). This indicates variety of the stable phases of dolomitic compositions in this pressure range. Moreover, Merlini et al. (2017) reported further transition of dolomite to IIIb phase observed at 36–115 GPa. Its structure corresponds to the *R*3 space group. An appearance of different structures in the pressure range for dolomite III stability indicates the possible existence of several structural modifications with similar energy. The structural transitions in dolomite show similarities with calcite I–II–III transitions. Indeed, $CaCO_3$ has several metastable polymorphs with close energy at high pressures.

At 115 GPa and 2200 °C, new phase dolomite IV was synthesized (Merlini et al., 2017). It is orthorhombic, space group *Pnma*, $a = 10.091(3)$. $b = 8.090(7)$. $c = 4.533(3)$ Å, $V = 370.1(4)$ Å ^{3}, at 115.2 GPa and ambient temperature. The structure is based on the presence of threefold C_3O_9 carbonate rings, with carbon in tetrahedral coordination. The structure of dolomite-IV presents similarities with the structural models proposed for the high-pressure polymorphs of $MgCO_3$.

Ab initio computations indicate that monoclinic *C*2/*c* Fe-bearing dolomite is more stable than single-cation carbonate mixtures at lower mantle pressures (Solomatova & Asimow, 2018); however, other structures were not considered, and an evolutionary search has not been performed.

Na_2CO_3–$CaCO_3$–$MgCO_3$. Phase relations in the Na_2CO_3–$CaCO_3$–$MgCO_3$ system have been studied in details at 3 GPa and 6 GPa (Figure 14.13a, b) (Podborodnikov et al., 2019; Shatskiy, Litasov, Sharygin, et al., 2016).

At 3 GPa and 700 °C, the system has five intermediate compounds: dolomite, Mg-bearing $Na_2Ca_4(CO_3)_5$ burbankite, $Na_2Ca_3(CO_3)_4$, $Na_4Ca(CO_3)_3$, and eitelite. As temperature increases to 800 °C, the system is complicated by an appearance of Ca-dolomite and Mg-bearing shortite, while $Na_2Ca_4(CO_3)_5$ disappears. $Na_4Ca(CO_3)_3$ decomposes to produce Na carbonate and nyerereite at 850 °C. The latter melts incongruently at 875 °C to form $Na_2Ca_3(CO_3)_4$. Incongruent melting of eitelite, producing magnesite and a liquid, occurs at 925 ± 25 °C. Mg-bearing shortite melts

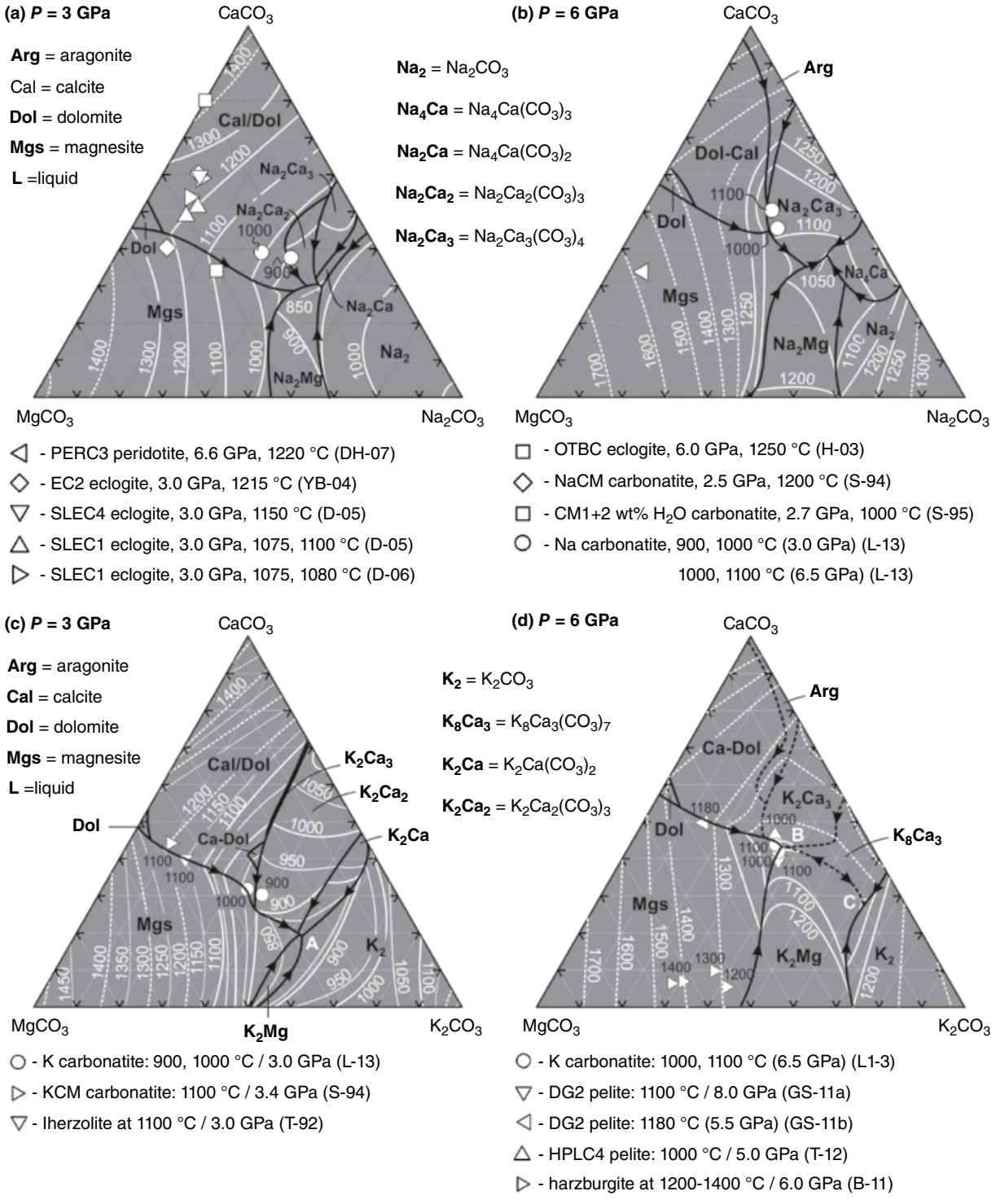

Figure 14.13 Melting phase relations in the Na_2CO_3–$MgCO_3$–$CaCO_3$ (a–b) and K_2CO_3–$MgCO_3$–$CaCO_3$ (c–d) ternary systems at 3 and 6 GPa (Podborodnikov et al., 2019; Shatskiy, Litasov, Palyanov, et al., 2016; Shatskiy, Litasov, Sharygin, et al., 2016). Black lines (dashed where inferred) are boundary lines and white lines (dashed where inferred) are liquidus isotherms with temperatures in °C. Compositions of carbonatite melts revealed from partial melting experiments in silicate–CO_2 systems are shown: DH-07 = (Dasgupta & Hirschmann, 2007a), YB-04 = (Yaxley & Brey, 2004), D-05 = (Dasgupta et al., 2005), D-06 = (Dasgupta et al., 2006), H-03 = (Hammouda, 2003), S-94 = (Sweeney, 1994), S-95 = (Sweeney et al., 1995), L-13 = (Litasov, Shatskiy, Ohtani, & Yaxley, 2013), T-92 = (Thibault et al., 1992), GS-11a and GS-11b = (Grassi & Schmidt, 2011a, 2011b), T-12 = (Tsuno et al., 2012), B-11 = (Brey et al., 2011). See electronic version for color representation of the figures in this book.

incongruently at about 950 °C producing $Na_2Ca_3(CO_3)_4$ and liquid. $Na_2Ca_3(CO_3)_4$ disappears at 1000 °C via incongruent melting to calcite + liquid. The liquidus projection of the studied ternary system has seven primary solidification phase regions for magnesite, dolomite-calcite solid solutions, $Na_2Ca_3(CO_3)_4$, Mg-bearing shortite, nyerereite, eitelite, and Na carbonate (Figure 14.13a). The system has six ternary peritectic points and one minimum on the liquidus at 825 °C and 52 Na_2CO_3 · 48 $(Ca_{0.62}Mg_{0.38})CO_3$. Since the system has a single eutectic at 3 GPa, there is no thermal barrier preventing continuous liquid fractionation from Na-poor to Na-rich dolomitic compositions more alkaline than eitelite and nyerereite.

At 6 GPa and 900–1000 °C, the system has four intermediate compounds: $Na_2Ca_4(CO_3)_5$ burbankite, $Na_2Ca_3(CO_3)_4$, $Na_4Ca(CO_3)_3$, and $Na_2Mg(CO_3)_2$ eitelite. The Na-Ca compounds dissolve noticeable amounts of Mg component, whereas eitelite dissolves a few percent of Ca component: $Na_2(Ca_{\geq 0.91}Mg_{\leq 0.09})_4(CO_3)_5$, $Na_2(Ca_{\geq 0.94}Mg_{\leq 0.06})_3(CO_3)_4$, $Na_4(Ca_{\geq 0.67}Mg_{\leq 0.33})(CO_3)_3$, and $Na_2(Mg_{\geq .93}Ca_{\leq 0.07})(CO_3)_2$. At 1050 °C, the system is complicated by the appearance of dolomite. Na-Ca burbankite decomposes at 1075 ± 25 °C via congruent melting between 1200 and 1250 °C producing aragonite plus $Na_2Ca_3(CO_3)_4$, $Na_4Ca(CO_3)_3$ and eitelite disappear. $Na_2Ca_3(CO_3)_4$ remains stable over the entire studied temperature range (900–1250 °C). The liquidus projection of the studied ternary system has eight primary solidification phase regions for magnesite, dolomite, calcite-dolomite solid solutions, aragonite, $Na_2Ca_3(CO_3)_4$, $Na_4Ca(CO_3)_3$, and Na_2CO_3 solid solutions (Figure 14.13b). The system has five ternary peritectic reaction points and one minimum on the liquidus at 1050 °C and $48Na_2CO_3{\cdot}52(Ca_{0.75}Mg_{0.25})CO_3$. The minimum point resembles a eutectic controlled by a four-phase reaction, by which a liquid transforms into three solid phases upon cooling: $Na_2(Ca_{0.94}Mg_{0.06})_3(CO_3)_4$, $Na_4(Ca_{0.67}Mg_{0.33})(CO_3)_3$, and $Na_2(Mg_{0.93}Ca_{0.07})(CO_3)_2$ eitelite.

Taking into account the data from the binary systems at low pressures, we can constrain Na-Ca-Mg double carbonate sequences upon pressure and temperature increase: $Na_2Ca_2(CO_3)_3$ (A*mm*2) shortite, $Na_2Ca(CO_3)_2$ ($P2_1ca$) nyerereite, $Na_2Mg(CO_3)_2$ ($R\bar{3}$) eitelite (0.1 GPa) → $Na_2(Ca_{0.97-0.98}Mg_{0.02-0.03})_4(CO_3)_5$ ($P6_3mc$). $Na_2(Ca_{\geq 0.91}Mg_{\leq 0.09})_3(CO_3)_4$ ($P1n1$). $Na_2(Ca_{\geq 0.81}Mg_{0\leq 0.19})(CO_3)_2$ ($R\bar{3}$) nyerereite, $Na_2(Ca_{0.77-0.93}Mg_{0.07-0.23})_2(CO_3)_3$ (A*mm*2) shortite, $Na_4(Ca_{0.90-0.98}Mg_{0.02-0.10})(CO_3)_3$ ($Ia3d$). $Na_2(Mg_{\geq 0.9}Ca_{0\leq 0.1})(CO_3)_2$ ($P2_1ca$) eitelite (3 GPa) → $Na_2(Ca_{\geq 0.87}Mg_{0\leq 0.13})_4(CO_3)_5$ ($P6_3mc$). $Na_2(Ca_{\geq 0.89}Mg_{\leq 0.11})_3(CO_3)_4$ ($P1n1$). $Na_4(Ca_{\geq .7}Mg_{0\leq 0.3})(CO_3)_3$ ($Ia3d$). $Na_2(Mg_{\geq 0.92}Ca_{0\leq 0.08})(CO_3)_2$ ($P2_1ca$) eitelite (6 GPa).

K_2CO_3–$CaCO_3$–$MgCO_3$. At 3 GPa, the liquidus projection of this ternary system has nine primary solidification phase regions for magnesite, dolomite, Ca-dolomite, calcite-dolomite solid solutions, $K_2Ca_3(CO_3)_4$, $K_2Ca_2(CO_3)_3$, $K_2Ca(CO_3)_2$ buetschliite, $K_2Mg(CO_3)_2$, and K_2CO_3 solid solutions containing up to 24 mol% $CaCO_3$ and less than 2 mol% $MgCO_3$ (Figure 14.13c). The system has six ternary peritectic reaction points and one eutectic at 825 ± 25 °C and $53K_2CO_3{\cdot}47Ca_{0.4}Mg_{0.6}CO_3$ (A) controlled by a four-phase reaction, where a liquid transforms into three solid phases on cooling: $K_2(Mg_{0.78}Ca_{0.22})(CO_3)_2$, $K_2(Ca_{0.70}Mg_{0.30})(CO_3)_2$ buetschliite, and $K_{1.70}Ca_{0.23}Mg_{0.07}CO_3$ solid solution.

At 6 GPa, the diagram has eight primary phase fields for magnesite, dolomite, calcite-dolomite solid solutions, aragonite, $K_2Ca_3(CO_3)_4$, $K_8Ca_3(CO_3)_7$, K_2CO_3, and $K_2Mg(CO_3)_2$. The system has four peritectic points and two eutectics near 1000 °C with compositions $36K_2CO_3{\cdot}64(Ca_{0.65}Mg_{0.35})CO_3$ (B) and $62K_2CO_3{\cdot}38Ca_{0.72}Mg_{0.28}CO_3$ (C) (Figure 14.13d). The eutectic (B) is controlled by three-phase assemblage of $K_2Ca_3(CO_3)_4$ + $K_8Ca_3(CO_3)_7$ + $K_2Mg(CO_3)_2$, whereas the eutectic (C) is controlled by three-phase assemblage of $K_8Ca_3(CO_3)_7$ + K_2CO_3 + $K_2Mg(CO_3)_2$.

Na_2CO_3–$FeCO_3$–$MgCO_3$. The ternary Na_2CO_3–$FeCO_3$–$MgCO_3$ system can be constrained at 6 GPa combining data from the corresponding binary systems: two systems with the intermediate $Na_2(Mg,Fe)(CO_3)_2$ phase, which melts congruently at the Mg-rich side and incongruently at the Fe-rich side, and the $(Mg,Fe)CO_3$ system with complete solid solutions. With decreasing $MgCO_3$ content, the eutectic shifts from 1225 °C and Na# = 48% toward lower temperatures and Na# =50%, where it changes to peritectic, which shifts to 1050 °C and Na# = 55%. The measurable amounts of $MgCO_3$ (up to 9 mol.%) and $FeCO_3$ (up to 3 mol.%) in Na_2CO_3 suggest an existence of the limited range of sodium carbonate solid solutions (Shatskiy, Rashchenko, et al., 2015).

K_2CO_3–$FeCO_3$–$MgCO_3$. Similarly, the ternary K_2CO_3–$FeCO_3$–$MgCO_3$ system at 6 GPa has two cotectic curves. One joining the two binary eutectics at 1250 °C and 48 mol.% K_2CO_3 at the Mg-side and at 1150 °C and 46 mol.% K_2CO_3 at the Fe-side. Another cotectic joins two eutectics at 1200 °C and 74 mol.% K_2CO_3 at the Mg-side and at 1100 °C and 65 mol.% K_2CO_3 at the Fe-side (Shatskiy, Litasov, Ohtani, et al., 2015).

14.4. IMPLICATIONS FOR MELTING IN THE DEEP EARTH'S MANTLE

14.4.1. Carbonates in the Complex Experimental Systems

Alkali-bearing carbonates were detected in several carbonated systems at P-T conditions relevant to the Earth's mantle: carbonated eclogite (Kiseeva et al., 2013; Thomson et al., 2016), pelite (Grassi & Schmidt, 2011b), and model Na- and K-bearing carbonatite (Litasov, Shatskiy, Ohtani, & Yaxley, 2013). Litasov, Shatskiy,

Ohtani, and Yaxley (2013) studied phase relations in model Na-rich (K# = 16, NaK# = 13, and Ca# = 54) and K-rich (K# = 70, NaK# = 9, and Ca# = 33) carbonatites at 3–21 GPa, where K# = 100·K/(K+Na) and NaK# = 100·(K_2O+Na_2O)/(K_2O+Na_2O+CaO+MgO+FeO). It has been found that Na is mainly hosted by Ca-rich crystalline carbonate in both systems over the entire pressure range, whereas K is mostly stored in $K_2Mg(CO_3)_2$. Using a new approach for carbonate analysis (see section 14.2) we re-analyzed and reinterpreted the data from Litasov, Shatskiy, Ohtani, and Yaxley (2013). Thus, unlike the original work, in the "Na-carbonatite" system, $Na_2Ca_4(CO_3)_5$ coexists with dolomite and eitelite at 3 GPa and 750 °C. This is consistent with the subsolidus phase assemblage, dolomite + $Na_2Ca_4(CO_3)_5$ + $Na_2Mg(CO_3)_2$, established in the ternary Na_2CO_3–$CaCO_3$–$MgCO_3$ system at 3 GPa and 700 °C (Podborodnikov et al., 2019). Similarly, at 6 GPa, the $Na_2Ca_3(CO_3)_4$ phase is stable instead of Na-aragonite reported in the original work.

Kiseeva et al. (2013) examined phase relations in carbonated eclogite (GA1-cc and Volga-cc) from 9 to 21 GPa. They found that the subsolidus carbonates are represented by magnesite and nearly pure aragonite to 9 GPa in Volga-cc and to 13 GPa in GA1-cc. At higher pressures, the subsolidus carbonates were represented by magnesite and Na-Ca carbonate with composition similar to that reported by Litasov, Shatskiy, Ohtani, and Yaxley (2013) (10–15 mol.% Na_2CO_3 + K_2CO_3, K# = 3–13, Ca# = 76–81). This carbonate was also identified as aragonite based on the Raman spectra. According to the binary and ternary carbonate systems at 3 and 6 GPa, $CaCO_3$ aragonite does not dissolve Na as well as K, Mg, and Fe. Instead, incorporation of Na into Ca-bearing carbonates form $Na_2Ca_4(CO_3)_5$, and $Na_2Mg(CO_3)_2$. However, the Raman spectra of $Na_2Ca_4(CO_3)_5$ exhibit the main bands in the same spectral region as aragonite, which can lead to misinterpretation. The Na-deficit relative to that required by the $Na_2Ca_4(CO_3)_5$ and $Na_2Mg(CO_3)_2$ stoichiometries is presumably due to the migration of Na under a stationary electron beam for both WDS and EDS analyses discussed in section 14.2.

Grassi and Schmidt (2011b) determined the phase relations in the carbonated pelite systems (DG2 and AM) from 5.5 to 23.5 GPa. They found that the decomposition of clinopyroxene at ≥ 16 GPa causes Na-Ca carbonate (16–20 mol.% Na_2CO_3 + K_2CO_3, K# = 1–7, Ca# = 73–84) to replace aragonite. Similar tendency was established in carbonated MORB composition. It was found that dissolution of Na-poor pyroxene components into coexisting garnet at pressures just above 13 GPa results in redistribution of Na from silicate (clinopyroxene) to Na-Ca carbonate $(Na_{0.97}K_{0.03})_2(Ca_{0.86}Mg_{0.11}Fe_{0.03})_4(CO_3)_5$, lowering the solidus by ~200 °C and yielding a Na-rich carbonatite melt (Thomson et al., 2016). The composition of this carbonate is very similar to the Na-Ca carbonate in Grassi and Schmidt (2011b) and to the $Na_2(Ca{\geq}_{0.87}Mg{\leq}_{0.13})_4(CO_3)_5$ compound established in the Na_2CO_3–$CaCO_3$–$MgCO_3$ system at 6 GPa and 900–1000 °C and at 3 GPa and 700 °C. The Na-Ca carbonate similar to $Na_2Ca_4(CO_3)_5$ was also detected among the run products from the experiment in natural Udachnaya-East kimberlite system at 6.5 GPa and 900 °C (Sharygin et al., 2015).

In the DG2 composition (dry pelite) at 22 and 23.5 GPa and temperature ≤ 1400 °C, carbonate with an approximate stoichiometry $Na_2Ca_2(CO_3)_3$ and almost no Mg, Fe, K has been identified (Grassi & Schmidt, 2011b). This carbonate resembles stoichiometry of Mg-free shortite, which is not stable at 3 GPa and ≥ 800 °C (Podborodnikov, Shatskiy, Arefiev, Rashchenko, et al., 2018) and at 6 GPa and ≥ 900 °C (Shatskiy et al., 2016b). In the Volga-cc composition (eclogite) at 21 GPa and 1200 °C, a carbonate with an empirical formula $(Na_{0.89}K_{0.11})_2(Ca_{0.68}Mg_{0.24}Fe_{0.08})(CO_3)_2$ was detected (Kiseeva et al., 2013). This carbonate resembles stoichiometry of nyerereite, which is stable at 3 GPa and 850 °C (Figure 14.7d). but disappears at 6 GPa and ≥ 900 °C (Figure 14.10) (Shatskiy et al., 2016b) according to the reaction: $Na_2Ca(CO_3)_2$ = $Na_4Ca(CO_3)_3$ + $Na_2Ca_3(CO_3)_4$ (Podborodnikov, Shatskiy, Arefiev, Rashchenko, et al., 2018). The appearance of carbonates with the same stoichiometries as shortite and neyrereite at pressures ≥ 21–22 GPa may indicate the existence of high-pressure polymorphs of these phases.

14.4.2. The Lower Temperature Stability Limits of Carbonatite Melts at 100–200 km Depths

Partial fusion of mantle peridotite/eclogite with CO_2 at depths shallower than 80 km produces silicate melts, whereas at greater depths the first incipient liquids, produced at much lower temperatures, are essentially carbonatitic (Wyllie & Huang, 1976; Yaxley & Brey, 2004; Yaxley & Green, 1994). Carbonatite melts, which are extremely effective in transporting incompatible elements, cause metasomatic modification of the shallow subcontinental mantle (Green & Wallace, 1988). The geochemical signatures of carbonatite metasomatism are commonly recognized in eclogite and peridotite xenoliths from alkaline basalts and kimberlites (Pokhilenko et al., 2015; Yaxley et al., 1991, 1998). It is therefore important to discuss the temperature range of carbonatite melt stability and their compositional trends at depths 100–200 km.

The lower temperature stability limits of dolomitic melt inferred from the liquidus-solidus minima on the join $CaCO_3$–$MgCO_3$ (CM–CO_2) are 1225 ± 25 °C at 3 GPa and 1400 °C at 6 GPa (Shatskiy et al., 2018). These temperatures coincide, within experimental uncertainty,

with the solidi of the CaO–MgO–SiO_2 ± Al_2O_3–CO_2 (CMS–CO_2 and CMAS–CO_2) systems modeling carbonated peridotite (Gudfinnsson & Presnall, 2005; Wyllie & Huang, 1976) (Figure 14.14). Similar to CM–CO_2, low-degree partial melting of CMS–CO_2 and CMAS–CO_2 yields silica-poor dolomitic melt. Sodium-bearing (NCMAS–CO_2) system and natural compositions (PERC and Hawaiian pyrolite) modeling carbonated peridotites at 3 GPa, revealed lower solidi temperatures, 1150 ± 50, 1090 ± 15, and ~1040 °C, respectively (Dasgupta & Hirschmann, 2006; Falloon & Green, 1989; Moore, 2012). The solidi of carbonated eclogites fall into the same temperature range: 1140 ± 40 °C (Yaxley & Brey, 2004), 1063–1113 °C (Dasgupta et al., 2005). As it can be seen in Figure 14.14, the experimentally inferred solidi of carbonated peridotites and eclogites cross the cratonic geotherms at depths ranging from 100 to 200 km and greater, yielding formation of essentially dolomitic melts. It was observed that near-solidus melts in the model peridotite–CO_2 and eclogite–CO_2 systems replicating natural compositions show strong enrichments in alkalis (Figure 14.13a) (Dasgupta & Hirschmann, 2006, 2007a; Dasgupta et al., 2004; Sweeney et al., 1995; Wallace & Green, 1988; Yaxley & Brey, 2004).

In the Na_2CO_3–$CaCO_3$–$MgCO_3$ system (NCM–CO_2) at 3 GPa, the compositions of melt in equilibrium with Ca-Mg carbonates show systematic variation with temperature from alkali-poor dolomitic at about 1225 °C, near the CM–CO_2 eutectic, toward sodic dolomitic (with 52 mol.% Na_2CO_3) at 825 °C, near the NCM–CO_2 minimum melting (Figure 14.14b). Sweeney (1994) has reported carbonatite melt with NaK# = 11, K# = 22, and Ca# = 45 established in equilibrium with phlogopite lherzolite at 1200 °C and 2.5 GPa in the NaCM system (Figure 14.13a). Later, Sweeney et al. (1995) have published new results on the phase relations of a "primary" sodic dolomitic carbonatite (CM1). determined by Wallace and Green (1988) to be in equilibrium with an amphibole lherzolite assemblage. They found that in the CM1 + 2 wt.% H_2O starting composition annealed at 2.7 GPa and 1000 °C, the carbonatite melt has NaK# = 26, K# = 2, and Ca# = 46. Litasov, Shatskiy, Ohtani, & Yaxley (2013) have reported experimental data on model sodic carbonatite, which is compositionally similar to a low-degree partial melt of carbonated eclogite at 3–10 GPa. We have reanalyzed the melt composition obtained by Litasov, Shatskiy, Ohtani, & Yaxley (2013) at 3 GPa and 900 °C and found that the melt has NaK# = 41, K# = 13, and Ca# = 64 (Figure 14.13a). These data show close agreement with the melt compositions observed in the related ternary carbonate systems.

The P-T plot in Figure 14.14b shows isopleths of Na_2CO_3 in the melt inferred from the carbonate phase

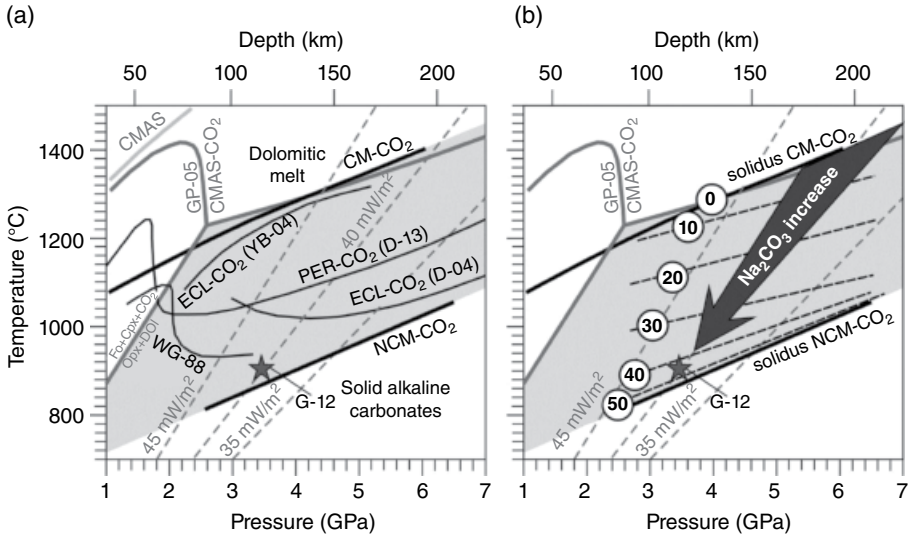

Figure 14.14 (a) Solidi of the carbonate and carbonate-silicate systems, compared with 35–45 mW/m^2 cratonic geotherms (gray dashed lines) (Hasterok & Chapman, 2011). G-12 (star) = P-T estimations for spinel harzburgite with primary Na-K-Ca-Mg carbonatite inclusions in metasomatic ilmenite (Giuliani et al., 2012). CM–CO_2 = $CaCO_3$–$MgCO_3$; NCM–CO_2 = Na_2CO_3–$CaCO_3$–$MgCO_3$; CMAS = CaO–MgO–SiO_2–Al_2O_3 (Gudfinnsson & Presnall, 1996); CMAS–CO_2 = CaO–MgO–SiO_2–Al_2O_3–CO_2 (Gudfinnsson & Presnall, 2005); D-13 = peridotite–CO_2 (Dasgupta et al., 2013); WG-88 = carbonate- and amphibole-bearing peridotite (0.3% H_2O and 0.5%–2.5% CO_2) (Wallace & Green, 1988); YB-04 = eclogite–CO_2 (Yaxley & Brey, 2004); D-04 = eclogite–CO_2 (Dasgupta et al., 2004). (b) P-T plot illustrating enrichment of magnesiocarbonatite melt with sodium during its upward percolation in subcratonic mantle lithosphere constrained. Black dashed lines are Na_2CO_3 isopleths with numbers indicating the Na_2CO_3 content in the melt in mol.%. See electronic version for color representation of the figures in this book.

diagrams at 3 and 6 GPa. The cratonic geotherms cross the isopleths, so that the carbonatite melt percolating upward via the continental mantle lithosphere should become progressively enriched by Na, evolving from alkali-poor dolomitic composition toward sodic dolomitic with Na_2CO_3 content 52 mol.% at the NCM–CO_2 solidus. These melts are buoyant and mobile, owing their low viscosity (Kono et al., 2014; Stagno et al., 2018). Upward percolation of such melts could yield metasomatic enrichment and wehrlitization in the shallower levels of subcratonic mantle lithosphere, documented in mantle xenoliths (Rudnick et al., 1993; Yaxley et al., 1998).

14.4.3. Implication of Carbonate Phase Diagrams to Mantle-Derived Carbonatite Inclusions

Kimberlites, lamproites, and alkaline basalts carry debris of the underlying lithospheric mantle. Many of these xenoliths show chemical, textural, and mineralogical evidences for metasomatism by fluids or melts within the mantle (Green & Wallace, 1988; Menzies & Hawkesworth, 1986). Giuliani et al. (2012) reported Na-K-Ca-Mg carbonatite melts preserved in primary multiphase inclusions hosted by metasomatic ilmenite grains in a spinel harzburgite from Bultfontein kimberlite (Kimberley, South Africa). Mineral thermometry indicates that the spinel harzburgite crystallized at ~860 °C, which corresponds to pressures near 3.5 GPa (~115 km) on a 40 mW/m^2 geotherm. This temperature corresponds to the low stability limit of Na-Ca-Mg carbonate melt according to the phase relations in the Na_2CO_3–$CaCO_3$–$MgCO_3$ system (Figure 14.14). The melts, detected by Giuliani et al. (2012). should be extremely enriched in alkalis, containing about 50 mol.% $(Na,K)_2CO_3$ and have Ca# ~60.

The sequence of Na-Ca and K-Ca carbonates established by phase diagram studies makes it possible to correctly interpret alkali carbonate inclusions in kimberlitic minerals. According to the phase relations at 6 GPa, shortite $Na_2Ca_2(CO_3)_3$ and nyerereite $Na_2Ca(CO_3)_2$, the double carbonates observed at 0.1 GPa (Cooper et al., 1975), are not stable in the deep mantle (Shatskiy, Sharygin, Litasov, et al., 2013). However, nyerereite is stable at the shallow mantle pressures at least up to 3 GPa and can be of the deep origin. Pure $Na_2Ca_2(CO_3)_3$ shortite is not stable at 3 GPa and ≥ 800 °C, however partial Mg substitution for Ca stabilizes shortite as a liquidus phase at 3 GPa and 800–900 °C. Consequently, the findings of nyerereite and shortite among daughter phases in melt inclusions in olivine from the sheared garnet peridotites (Golovin et al., 2017) are consistent with their mantle origin at least at pressures of kimberlite magma ascent to the surface.

14.4.4. Carbonates in the Lower Mantle

The highly reduced nature of the lower mantle and, possibly, part of the upper mantle and transition zone indicates the instability of carbonates in the deep Earth's interior. At the conditions of the iron-wüstite buffer, which are claimed for most of the mantle (Frost & McCammon, 2008), diamond or Fe-carbide should be the major host for carbon.

Ca-Mg carbonate cannot coexist with metallic iron even at pressures of the D" layer at CMB and react to form Fe-carbide or diamond (Dorfman et al., 2018; Martirosyan et al., 2019). However, this may not be the case for Fe-carbonate and its related compounds stable under the lower mantle conditions. Moreover, oxidation state of the mantle can be strongly heterogenous. Oxidized subducting slabs or mantle wedge materials can be entrained in convective mixing but can remain heterogenous for a long time due to sluggish kinetics of exchange reactions, even in partially molten matrices. In this case, carbonate or carbonatite melt can survive in the deep mantle, even when surrounded by the reduced material of the ambient mantle (Martirosyan et al., 2016) and be submerged as deep as CMB. This possibility is clearly indicated by carbonate inclusions in superdeep diamonds originating from the uppermost lower mantle (Brenker et al., 2007; Kaminsky, 2012).

There are several possible scenarios for the interaction of subducted material with rocks in the D" layer and the CMB. In the first model, subducted rocks will never appear in contact with the CMB and metallic iron, but will interact only with the uppermost layer of dense D" rocks before being incorporated in mantle convection or plumes. In this case, subducted carbonates will be mostly transformed to diamond (Maeda et al., 2017). A second scenario assumes active reaction of subduction materials with the D" and even with metal from the core. In this case, we may expect formation of diamond in the top portions of the slab/D′′ contact layer and Fe-carbide if carbonate or diamond appears in the direct contact with metallic Fe (Dorfman et al., 2018; Martirosyan et al., 2019) (Figure 14.15).

If both hydrogen and carbon penetrate to the D" depths with subduction slabs they can be remobilized. The reactions of Fe with mixed carbon and hydrogen have been modeled only theoretically. Belonoshko et al. (2015) showed formation of hydrocarbons from the interaction of Fe with C–O–H or H_2O–CO_2 fluids. These hydrocarbons can serve as fusible components for the formation and movement of mantle plumes. It is important to note that Fe is preferentially bonded to carbon and oxygen so that these elements may be consumed by the core. In contrast, hydrogen does not form bonds with Fe and is mostly involved into plume recycling (Litasov & Shatskiy, 2018). This observation has not yet been verified experimentally.

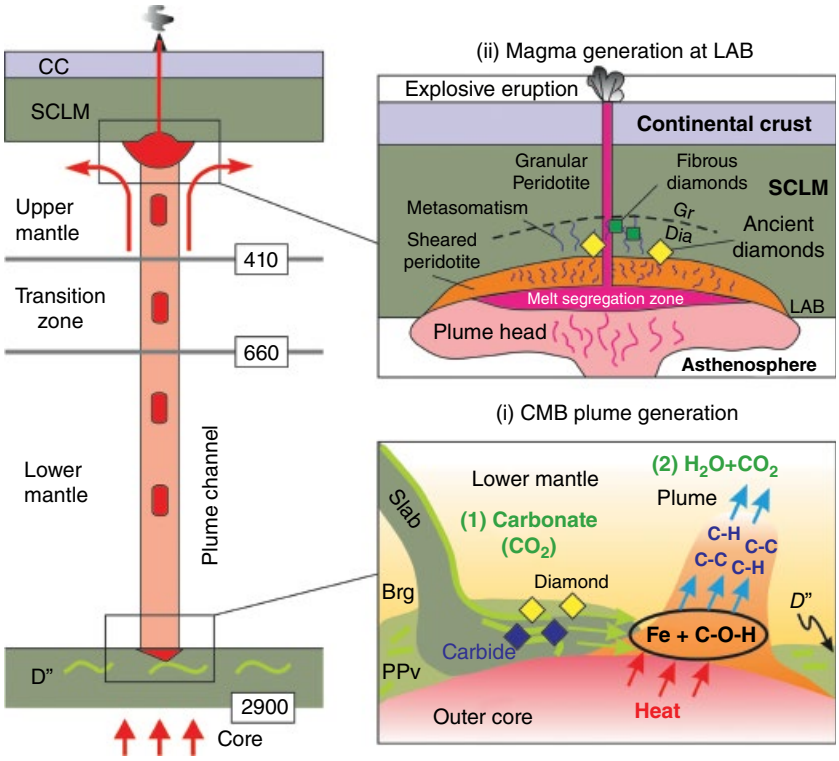

Figure 14.15 Schematic model for mantle plume generation at the core-mantle boundary (CMB) associated with burial and remobilization of carbon-bearing compounds. Right panels, bottom to top: (i) Carbonate reduction at the CMB and generation of the CMB plume. In hydrogen-free conditions carbonates are reduced to diamond in contact with reduced lithologies of the D″ layer and to carbide if they encounter metallic Fe. In this case, remobilization of carbon from the CMB is difficult. In hydrous conditions (H_2O+CO_2), carbon and hydrogen react with metallic iron or reduced rocks to form hydrocarbons (shown as C–C and C–H bonds), which can enhance formation of mantle plumes (Belonoshko et al., 2015; Martirosyan et al., 2019). (ii) Carbonatite or hydrocarbon-bearing hydrous melts approach the lithosphere-asthenosphere boundary (LAB), where they can solidify to form the source for later magmatism or, in case of high enough capacity, immediately cause lithosphere erosion, deformation, and metasomatism with formation of carbonatite, kimberlite, or other alkaline magmas. The examples for kimberlite magmas are shown in Pokhilenko et al., 2015; Sharygin et al., 2015; and Shatskiy, Litasov, et al., 2017). Abbreviations: OC = oceanic crust, CC = continental crust, SCLM = subcontinental lithospheric mantle, Gr = graphite, Dia = diamond, Brg = bridgmanite, Ppv = postperovskite $(Mg,Fe)SiO_3$. See electronic version for color representation of the figures in this book.

ACKNOWLEDGMENTS

This work was supported by Russian Science Foundation (No 14-17-00609-P) and performed under the Deep Carbon Observatory program.

REFERENCES

Agashev, A. M., D. A. Ionov, N. P. Pokhilenko, A. V. Golovin, Y. Cherepanova, & I. S. Sharygin (2013). Metasomatism in lithospheric mantle roots: Constraints from whole-rock and mineral chemical composition of deformed peridotite xenoliths from kimberlite pipe Udachnaya, *Lithos*, *160–161*, 201–215.

Al-Shemali, M., & A. I. Boldyrev (2002). Search for ionic orthocarbonates: Ab initio study of Na_4CO_4. *The Journal of Physical Chemistry A*, *106*, 8951–8954.

Arapan, S., J. S. De Almeida, & R. Ahuja (2007). Formation of sp^3 hybridized bonds and stability of $CaCO_3$ at very high pressure. *Physical Review Letters*, *98*, 268501.

Arefiev, A. V., A. Shatskiy, I. V. Podborodnikov, S. V. Rashchenko, A. D. Chanyshev, & K. D. Litasov (2019). The system K_2CO_3–$CaCO_3$ at 3 GPa: link between phase relations and variety of K–Ca double carbonates at ≤ 0.1 and 6 GPa. *Physics and Chemistry of Minerals*, *46*, 229–244.

Arefiev, A. V., A. Shatskiy, I. V. Podborodnikov, S. V. Rashchenko, & K. D. Litasov (2018). The system K_2CO_3–$MgCO_3$ at 3 GPa. *High Pressure Research*, *38*, 422–439.

Bagdassarov, N. S., & A. B. Slutskii (2003). Phase transformations in calcite from electrical impedance measurements, *Phase Transitions*, *76*, 1015–1028.

Bayarjargal, L., C.-J. Fruhner, N. Schrodt, & B. Winkler (2018). $CaCO_3$ phase diagram studied with Raman spectroscopy at pressures up to 50 GPa and high temperatures and DFT modeling. *Physics of the Earth and Planetary Interiors*, *281*, 31–45.

Becht, H. Y., & R. Struikmans (1976). A monoclinic high-temperature modification of potassium carbonate. *Acta Crystallographica B*, *32*, 3344–3346.

Belonoshko, A. B., T. Lukinov, A. Rosengren, T. Bryk, & K. D. Litasov (2015). Synthesis of heavy hydrocarbons at the core-mantle boundary, *Scientific Reports*, *5*, 18382.

Bobrovsky, S. V., V. M. Gogolev, B. V. Zamyshlyaev, V. P. Lozhkina, and V. V. Rasskazov (1976). The study of thermal decomposition influence on the spallation velocity for strong shock waves in solids. *Soviet Mining Science*, *3*, 49–57.

Boulard, E., N. Menguy, A. L. Auzende, K. Benzerara, H. Bureau, D. Antonangeli, A. Corgne, et al. (2012). Experimental investigation of the stability of Fe-rich carbonates in the lower mantle. *Journal of Geophysical Research-Solid Earth*, *117*, B02208, doi: 10.1029/2011jb 008733.

Brenker, F. E., C. Vollmer, L. Vincze, B. Vekemans, A. Szymanski, K. Janssens, I. Szaloki, et al. (2007). Carbonates from the lower part of transition zone or even the lower mantle. *Earth and Planetary Science Letters*, *260*, 1–9.

Brey, G. P., V. K. Bulatov, & A. V. Girnis (2011). Melting of K-rich carbonated peridotite at 6–10 GPa and the stability of K-phases in the upper mantle. *Chemical Geology*, *281*, 333–342.

Brey, G. P., & T. Kohler (1990). Geothermobarometry in four-phase lherzolites II. New thermobarometers, and practical assessment of existing thermobarometers. *Journal of Petrology*, *31*, 1353–1378.

Buob, A., R. W. Luth, M. W. Schmidt, & P. Ulmer (2006). Experiments on $CaCO_3$–$MgCO_3$ solid solutions at high pressure and temperature, *American Mineralogist*, *91*, 435–440.

Bykova, E., L. Dubrovinsky, N. Dubrovinskaia, M. Bykov, C. McCammon, S. Ovsyannikov, H.-P. Liermann, et al. (2016). Structural complexity of simple Fe_2O_3 at high pressures and temperatures. *Nature Communications*, *7*, 10661.

Byrnes, A. P., & P. J. Wyllie (1981). Subsolidus and melting relations for the join $CaCO_3$–$MgCO_3$ at 10 kbar, *Geochimica et Cosmochimica Acta*, *45*, 321–328.

Cancarevic, Z. P., J. C. Schon, & M. Jansen (2007). Possible existence off alkali metal orthocarbonates at high pressure. *Chemistry-a European Journal*, *13*, 7330–7348.

Cerantola, V., E. Bykova, I. Kupenko, M. Merlini, L. Ismailova, C. McCammon, M. Bykov, et al. (2017). Stability of iron-bearing carbonates in the deep Earth's interior. *Nature Communications*, *8*, 15960.

Cooper, A. F., J. Gittins, & O. F. Tuttle (1975). The system Na_2CO_3–K_2CO_3–$CaCO_3$ at 1 kilobar and its significance in carbonatite petrogenesis. *American Journal of Science*, *275*, 534–560.

Dalton, J. A., & D. C. Presnall (1998). Carbonatitic melts along the solidus of model lherzolite in the system CaO–MgO–Al_2O_3–SiO_2–CO_2 from 3 to 7 GPa. *Contributions to Mineralogy and Petrology*, *131*, 123–135.

Dasgupta, R. (2013). Ingassing, storage, and outgassing of terrestrial carbon through geologic time. *Reviews in Mineralogy and Geochemistry*, *75*, 183–229.

Dasgupta, R., & M. M. Hirschmann (2006). Melting in the Earth's deep upper mantle caused by carbon dioxide. *Nature*, *440*, 659–662.

Dasgupta, R., & M. M. Hirschmann (2007a). Effect of variable carbonate concentration on the solidus of mantle peridotite. *American Mineralogist*, *92*, 370–379.

Dasgupta, R., & M. M. Hirschmann (2007b). A modified iterative sandwich method for determination of near-solidus partial melt compositions. II. Application to determination of near-solidus melt compositions of carbonated peridotite. *Contributions to Mineralogy and Petrology*, *154*, 647–661.

Dasgupta, R., & M. M. Hirschmann (2010). The deep carbon cycle and melting in Earth's interior. *Earth and Planetary Science Letters*, *298*, 1–13.

Dasgupta, R., M. M. Hirschmann, & N. Dellas (2005). The effect of bulk composition on the solidus of carbonated eclogite from partial melting experiments at 3 GPa, *Contributions to Mineralogy and Petrology*, *149*, 288–305.

Dasgupta, R., M. M. Hirschmann, & K. Stalker (2006). Immiscible transition from carbonate-rich to silicate-rich melts in the 3 GPa melting interval of eclogite plus CO_2 and genesis of silica-undersaturated ocean island lavas. *Journal of Petrology*, *47*, 647–671.

Dasgupta, R., M. M. Hirschmann, & A. C. Withers (2004). Deep global cycling of carbon constrained by the solidus of anhydrous, carbonated eclogite under upper mantle conditions, *Earth and Planetary Science Letters. 227*, 73–85.

Dasgupta, R., A. Mallik, K. Tsuno, A. C. Withers, G. Hirth, & M. M. Hirschmann (2013). Carbon-dioxide-rich silicate melt in the Earth's upper mantle. *Nature*, *493*, 211–215.

Davidson, P. M. (1994). Ternary iron, magnesium, calcium carbonates: A thermodynamic model for dolomite as an ordered derivative of calcite-structure solutions. *American Mineralogist*, *79*, 332–339.

Depater, C. J. (1979). Disordered structure of Na_2CO_3 at 400 °C, *Physica B & C*, *96*, 89–95.

Dewaele, A., G. Fiquet, & P. Gillet (1998). Temperature and pressure distribution in the laser-heated diamond-anvil cell. *Review of Scientific Instruments*, *69*, 2421–2426.

Dinnebier, R. E., S. Vensky, M. Jansen, & J. C. Hanson (2005). Crystal structures and topological aspects of the high-temperature phases and decomposition products of the alkali-metal oxalates $M_2(C_2O_4)$ (M = K, Rb, Cs). *Chemistry-a European Journal*, *11*, 1119–1129.

Dobrzhinetskaya, L. F., R. Wirth, & H. W. Green (2006). Nanometric inclusions of carbonates in Kokchetav diamonds from Kazakhstan: A new constraint for the depth of metamorphic diamond crystallization. *Earth and Planetary Science Letters*, *243*, 85–93.

Dorfman, S. M., J. Badro, F. Nabiei, V. B. Prakapenka, M. Cantoni, & P. Gillet (2018). Carbonate stability in the reduced lower mantle. *Earth and Planetary Science Letters*, *489*, 84–91.

Dusek, M., G. Chapuis, M. Meyer, & V. Petricek (2003). Sodium carbonate revisited. *Acta Crystallographica B*, *59*, 337–352.

Eitel, W., & W. Skaliks (1929). Some double carbonates of alkali and earth alkali. *Zeitschrift Fur Anorganische Und Allgemeine Chemie*, *183*, 263–286.

Falloon, T. J., & D. H. Green (1989). Solidus of carbonated fertile peridotite. *Earth and Planetary Science Letters*, *94*, 364–370.

Foley, S. F., G. M. Yaxley, A. Rosenthal, S. Buhre, E. S. Kiseeva, R. P. Rapp, & D. E. Jacob (2009). The composition of near-solidus

melts of peridotite in the presence of CO_2 and H_2O between 40 and 60 kbar. *Lithos*, *112*(S1). 274–283.

Franzolin, E., M. W. Schmidt, & S. Poli (2011). Ternary Ca–Fe–Mg carbonates: Subsolidus phase relations at 3.5 GPa and a thermodynamic solid solution model including order/disorder. *Contributions to Mineralogy and Petrology*, *161*, 213–227.

Frost, D. J., & C. A. McCammon (2008). The redox state of Earth's mantle. *Annual Review of Earth and Planetary Sciences*, *36*, 389–420.

Gavryushkin, P. N., A. Behtenova, Z. I. Popov, V. V. Bakakin, A. Y. Likhacheva, K. D. Litasov, & A. Gavryushkin (2016). Toward analysis of structural changes common for alkaline carbonates and binary compounds: Prediction of high-pressure structures of Li_2CO_3, Na_2CO_3, and K_2CO_3. *Crystal Growth & Design*, *16*, 5612–5617.

Gavryushkin, P. N., N. S. Martirosyan, T. M. Inerbaev, Z. I. Popov, S. V. Rashchenko, A. Y. Likhacheva, S. S. Lobanov, et al. (2017). Aragonite-II and $CaCO_3$-VII: new high-pressure, high-temperature polymorphs of $CaCO_3$. *Crystal Growth & Design*, *17*, 6291–6296.

Ghosh, S., E. Ohtani, K. D. Litasov, & H. Terasaki (2009). Solidus of carbonated peridotite from 10 to 20 GPa and origin of magnesiocarbonatite melt in the Earth's deep mantle. *Chemical Geology*, *262*, 17–28.

Giuliani, A., V. S. Kamenetsky, D. Phillips, M. A. Kendrick, B. A. Wyatt, & K. Goemann (2012). Nature of alkali-carbonate fluids in the sub-continental lithospheric mantle. *Geology*, *40*, 967–970.

Goldsmith, J. R., D. L. Graf, J. Witters, & D. A. Northrop (1962). Studies in the system $CaCO_3$–$MgCO_3$–$FeCO_3$: 1. Phase relations. 2. A method for major-element spectrochemical analysis. 3. Compositions of some Ferroan dolomites. *Journal of Geology*, *70*, 659–688.

Goldsmith, J. R., & H. C. Heard (1961). Subsolidus phase relations in the system $CaCO_3$-$MgCO_3$. *Journal of Geology*, *69*, 45–74.

Golovin, A. V., I. S. Sharygin, V. S. Kamenetsky, A. V. Korsakov, & G. M. Yaxley (2018). Alkali-carbonate melts from the base of cratonic lithospheric mantle: links to kimberlites. *Chemical Geology*, *483*, 261–274.

Golovin, A. V., I. S. Sharygin, & A. V. Korsakov (2017). Origin of alkaline carbonates in kimberlites of the Siberian craton: Evidence from melt inclusions in mantle olivine of the Udachnaya-East pipe. *Chemical Geology*, *455*, 357–375.

Golubkova, A., M. Merlini, & M. W. Schmidt (2015). Crystal structure, high-pressure, and high-temperature behavior of carbonates in the $K_2Mg(CO_3)_2$–$Na_2Mg(CO_3)_2$ join. *American Mineralogist*, *100*, 2458–2467.

Graf, D. L., & J. R. Goldsmith (1955). Dolomite-magnesian calcite relations at elevated temperatures and CO_2 pressures. *Geochimica et Cosmochimica Acta*, *7*, 109–128.

Grassi, D., & M. W. Schmidt (2011a). Melting of carbonated pelites at 8–13 GPa: generating K-rich carbonatites for mantle metasomatism. *Contributions to Mineralogy and Petrology*, *162*, 169–191.

Grassi, D., & M. W. Schmidt (2011b). The melting of carbonated pelites from 70 to 700 km depth. *Journal of Petrology*, *52*, 765–789.

Green, D. H., & M. E. Wallace (1988). Mantle metasomatism by ephemeral carbonatite melts. *Nature*, *336*, 459–462.

Gudfinnsson, G. H., & D. C. Presnall (1996). Melting relations of model lherzolite in the system CaO-MgO-Al_2O_3-SiO_2 at 2.4–3.4 GPa and the generation of komatiites. *Journal of Geophysical Research: Solid Earth*, *101*, 27701–27709.

Gudfinnsson, G. H., & D. C. Presnall (2005). Continuous gradations among primary carbonatitic, kimberlitic, melilititic, basaltic, picritic, and komatiitic melts in equilibrium with garnet lherzolite at 3–8 GPa. *Journal of Petrology*, *46*, 1645–1659.

Hammouda, T. (2003). High-pressure melting of carbonated eclogite and experimental constraints on carbon recycling and storage in the mantle. *Earth and Planetary Science Letters*, *214*, 357–368.

Harker, R. I., & O. F. Tuttle (1955a). Studies in the system CaO–MgO–CO_2. 1. The thermal dissociation of calcite, dolomite and magnesite. *American Journal of Science*, *253*, 209–224.

Harker, R. I., & O. F. Tuttle (1955b). Studies in the system CaO–MgO–CO_2: 2. Limits of solid solution along the binary join, $CaCO_3$–$MgCO_3$. *American Journal of Science*, *253*, 274–282.

Harris, M. J., & M. T. Dove (1995). Lattice melting at structural phase-transitions. *Modern Physics Letters B*, *9*, 67–85.

Harris, M. J., & E. K. H. Salje (1992). The incommensurate phase of sodium carbonate: An infrared absorption study. *Journal of Physics-Condensed Matter*, *4*, 4399–4408.

Hasterok, D., & D. Chapman (2011). Heat production and geotherms for the continental lithosphere. *Earth and Planetary Science Letters*, *307*, 59–70.

Hermann, J., U. Troitzsch, & D. Scott (2016). Experimental subsolidus phase relations in the system $CaCO_3$–$CaMg(CO_3)_2$ up to 6.5 GPa and implications for subducted marbles. *Contributions to Mineralogy and Petrology*, *171*, 84.

Hernlund, J., K. Leinenweber, D. Locke, & J. A. Tyburczy (2006). A numerical model for steady-state temperature distributions in solid-medium high-pressure cell assemblies. *American Mineralogist*, *91*, 295–305.

Hesse, K.-F., & B. Simons (1982). Crystalstructure of synthetic $K_2Mg(CO_3)_2$. *Zeitschrift fur Kristallographie*, *161*, 289–292.

Irving, A., & P. Wyllie (1973). Melting relationships in CaO–CO_2 and MgO–CO_2 to 36 kilobars with comments on CO_2 in the mantle. *Earth and Planetary Science Letters*, *20*, 220–225.

Irving, A. J., & P. J. Wyllie (1975). Subsolidus and melting relationships for calcite, magnesite and the join $CaCO_3$–$MgCO_3$ to 36 kb. *Geochimica et Cosmochimica Acta*, *39*, 35–53.

Ishizawa, N., H. Setoguchi, & K. Yanagisawa (2013). Structural evolution of calcite at high temperatures: Phase V unveiled. *Scientific Reports*, *3*, 02832.

Isshiki, M., T. Irifune, K. Hirose, S. Ono, Y. Ohishi, T. Watanuki, E. Nishibori, et al. (2004). Stability of magnesite and its high-pressure form in the lowermost mantle. *Nature*, *427*, 60–63.

Ivanov, B. A., & A. Deutsch (2002). The phase diagram of $CaCO_3$ in relation to shock compression and decomposition. *Physics of the Earth and Planetary Interiors*, *129*, 131–143.

Jablon, B. M., & O. Navon (2016). Most diamonds were created equal. *Earth and Planetary Science Letters*, *443*, 41–47.

Johnston, F. K. B., A. V. Turchyn, & M. Edmonds (2011). Decarbonation efficiency in subduction zones: Implications for warm Cretaceous climates. *Earth and Planetary Science Letters*, *303*, 143–152.

Jones, A. G., I. J. Ferguson, A. D. Chave, R. L. Evans, & G. W. McNeice (2001). Electric lithosphere of the Slave craton. *Geology*, *29*, 423–426.

Jones, A. G., P. Lezaeta, I. J. Ferguson, A. D. Chave, R. L. Evans, X. Garcia, & J. Spratt (2003). The electrical structure of the Slave craton. *Lithos*, *71*, 505–527.

Kamenetsky, V. S., H. Grütter, M. B. Kamenetsky, & K. Gömann (2013). Parental carbonatitic melt of the Koala kimberlite (Canada): Constraints from melt inclusions in olivine and Cr-spinel, and groundmass carbonate. *Chemical Geology*, *353*, 96–111.

Kamenetsky, V. S., M. B. Kamenetsky, Y. Weiss, O. Navon, T. F. D. Nielsen, & T. P. Mernagh (2009). How unique is the Udachnaya-East kimberlite? Comparison with kimberlites from the Slave Craton (Canada) and SW Greenland. *Lithos*, *112*(S1). 334–346.

Kaminsky, F. (2012). Mineralogy of the lower mantle: A review of 'super-deep' mineral inclusions in diamond. *Earth-Science Reviews*, *110*, 127–147.

Kaminsky, F. V., I. D. Ryabchikov, & R. Wirth (2016). A primary natrocarbonatitic association in the Deep Earth. *Mineralogy and Petrology*, *110*, 387–398.

Kang, N., M. W. Schmidt, S. Poli, J. A. Connolly, & E. Franzolin (2016). Melting relations in the system $FeCO_3$–$MgCO_3$ and thermodynamic modelling of Fe–Mg carbonate melts. *Contributions to Mineralogy and Petrology*, *171*, 74.

Kang, N., M. W. Schmidt, S. Poli, E. Franzolin, & J.A.D. Connolly (2015). Melting of siderite to 20 GPa and thermodynamic properties of $FeCO_3$-melt. *Chemical Geology*, *400*, 34–43.

Katsura, T., & E. Ito (1990). Melting and subsolidus phase relations in the $MgSiO_3$–$MgCO_3$ system at high pressures: Implications to evolution of the Earth's atmosphere. *Earth and Planetary Science Letters*, *99*, 110–117.

Kavner, A., & C. Nugent (2008). Precise measurements of radial temperature gradients in the laser-heated diamond anvil cell. *Review of Scientific Instruments*, *79*, 024902.

Kelemen, P. B., & C. E. Manning (2015). Reevaluating carbon fluxes in subduction zones, what goes down, mostly comes up. *Proceedings of the National Academy of Sciences*, *112*, E3997–E4006.

Kennedy, C. S., & G. C. Kennedy (1976). The equilibrium boundary between graphite and diamond. *Journal of Geophysical Research*, *81*, 2467–2470.

Kerley, G. I. (1989). Equations of state for calcite minerals: I. Theoretical model for dry calcium carbonate. *High Pressure Research*, *2*, 29–47.

Kerrick, D. M., & J. A. D. Connolly (2001). Metamorphic devolatilization of subducted marine sediments and the transport of volatiles into the Earth's mantle. *Nature*, *411*, 293–296.

Keshav, S., A. Corgne, G. H. Gudfinnsson, M. Bizimis, W. F. McDonough, & Y. W. Fei (2005). Kimberlite petrogenesis: Insights from clinopyroxene–melt partitioning experiments at 6 GPa in the CaO–MgO–Al_2O_3–SiO_2–CO_2 system. *Geochimica et Cosmochimica Acta*, *69*, 2829–2845.

Kiseeva, E. S., K. D. Litasov, G. M. Yaxley, E. Ohtani, & V. S. Kamenetsky (2013). Melting and phase relations of carbonated eclogite at 9–21 GPa and the petrogenesis of alkali-rich melts in the deep mantle. *Journal of Petrology*, *54*(8). 1555–1583.

Klein-BenDavid, O., A. M. Logvinova, M. Schrauder, Z. V. Spetius, Y. Weiss, E. H. Hauri, F. V. Kaminsky, et al. (2009). High-Mg carbonatitic microinclusions in some Yakutian diamonds: a new type of diamond-forming fluid. *Lithos*, *112*(S2). 648–659.

Klement, W., & L. H. Cohen (1975). Solid-solid and solid-liquid transitions in K_2CO_3, Na_2CO_3 and Li_2CO_3: Investigations to ≥ 5 kbar by differential thermal analysis; thermodynamics and structural correlations. *Berichte der Bunsengesellschaft für physikalische Chemie*, *79*, 327–334.

Koch-Müller, M., S. Jahn, N. Birkholz, E. Ritter, & U. Schade (2016). Phase transitions in the system $CaCO_3$ at high P and T determined by in situ vibrational spectroscopy in diamond anvil cells and first-principles simulations. *Physics and Chemistry of Minerals*, *43*, 545–561.

Kono, Y., C. Kenney-Benson, D. Hummer, H. Ohfuji, C. Park, G. Shen, Y. Wang, et al. (2014). Ultralow viscosity of carbonate melts at high pressures. *Nature Communications*, *5*, 5091.

Kopylova, M., O. Navon, L. Dubrovinsky, & G. Khachatryan (2010). Carbonatitic mineralogy of natural diamond-forming fluids. *Earth and Planetary Science Letters*, *291*, 126–137.

Kröger, C., K. W. Illner, & W. Graeser (1943). Über die systeme alkalioxyd CaO–Al_2O_3–SiO_2–CO_2. XI. die reaktionsdrucke im system K_2O–CaO–SiO_2–CO_2. *Zeitschrift Fur Anorganische Und Allgemeine Chemie*, *251*, 270–284.

Lavina, B., P. Dera, R. T. Downs, V. Prakapenka, M. Rivers, S. Sutton, & M. Nicol (2009). Siderite at lower mantle conditions and the effects of the pressure-induced spin-pairing transition. *Geophysical Research Letters*, *36*, L23306, doi: 10.1029/2009gl039652.

Lavrent'ev, Y. G., N. S. Karmanov, & L. V. Usova (2015). Electron probe microanalysis of minerals: Microanalyzer or scanning electron microscope? *Russian Geology and Geophysics*, *56*, 1154–1161.

Li, X., Z. Zhang, J. F. Lin, H. Ni, V. B. Prakapenka, & Z. Mao (2018). New high-pressure phase of $CaCO_3$ at the topmost lower mantle: Implication for the deep-mantle carbon transportation. *Geophysical Research Letters*, *45*, 1355–1360.

Li, Z. (2015). Melting and structural transformations of carbonates and hydrous phases in Earth's mantle (PhD thesis, 126 pp). The University of Michigan.

Li, Z., J. Li, R. Lange, J. Liu, & B. Militzer (2017). Determination of calcium carbonate and sodium carbonate melting curves up to Earth's transition zone pressures with implications for the deep carbon cycle. *Earth and Planetary Science Letters*, *457*, 395–402.

Litasov, K. D. (2011). Physicochemical conditions for melting in the Earth's mantle containing a C–O–H fluid (from experimental data). *Russian Geology and Geophysics*, *51*, 475–492.

Litasov, K. D., & E. Ohtani (2009). Solidus and phase relations of carbonated peridotite in the system CaO–Al_2O_3–MgO–SiO_2–Na_2O–CO_2 to the lower mantle depths. *Physics of the Earth and Planetary Interiors*, *177*, 46–58.

Litasov, K. D., & E. Ohtani (2010). The solidus of carbonated eclogite in the system $CaO–Al_2O_3–MgO–SiO_2–Na_2O–CO_2$ to 32 GPa and carbonatite liquid in the deep mantle. *Earth and Planetary Science Letters*, *295*, 115–126.

Litasov, K. D., & A. Shatskiy (2018). Carbon-bearing magmas in the Earth's deep interior. In Y. Kono and C. Sanloup (Eds.), *Magmas Under Pressure* (pp. 43–82), Elsevier.

Litasov, K. D., A. Shatskiy, P. N. Gavryushkin, A. E. Bekhtenova, P. I. Dorogokupets, B. S. Danilov, Y. Higo, et al. (2017). PVT equation of state of $CaCO_3$ aragonite to 29 GPa and 1673 K: In situ X-ray diffraction study. *Physics of the Earth and Planetary Interiors*, *265*, 82–91.

Litasov, K. D., A. Shatskiy, & E. Ohtani (2013). Earth's mantle melting in the presence of C-O-H-bearing fluid. In S. Karato (Ed.), *Physics and Chemistry of the Deep Earth* (pp. 38–65). New York: Wiley.

Litasov, K. D., A. Shatskiy, E. Ohtani, & G. M. Yaxley (2013). Solidus of alkaline carbonatite in the deep mantle. *Geology*, *41*, 79–82.

Litasov, K. D., A. F. Shatskiy, & N. P. Pokhilenko (2011). Phase relations and melting in the systems of peridotite–$H_2O–CO_2$ and eclogite–$H_2O–CO_2$ at pressures up to 27 GPa. *Doklady Earth Sciences*, *437*, 498–502.

Liu, J., J.-F. Lin, & V. B. Prakapenka (2015). High-pressure orthorhombic ferromagnesite as a potential deep-mantle carbon carrier. *Scientific Reports*, *5*, 7640.

Liu, Q., T. J. Tenner, & R. A. Lange (2007). Do carbonate liquids become denser than silicate liquids at pressure? Constraints from the fusion curve of K_2CO_3 to 3.2 GPa. *Contributions to Mineralogy and Petrology*, *153*, 55–66.

Lobanov, S. S., X. Dong, N. S. Martirosyan, A. I. Samtsevich, V. Stevanovic, P. N. Gavryushkin, K. D. Litasov, et al. (2017). Raman spectroscopy and x-ray diffraction of sp^3 $CaCO_3$ at lower mantle pressures. *Physical Review B*, *96*, 104101.

Lobanov, S. S., A. F. Goncharov, & K. D. Litasov (2015). Optical properties of siderite ($FeCO_3$) across the spin transition: Crossover to iron-rich carbonates in the lower mantle. *American Mineralogist*, *100*, 1059–1064.

Logvinova, A. M., R. Wirth, A. A. Tomilenko, V. P. Afanas'ev, & N. V. Sobolev (2011). The phase composition of crystal-fluid nanoinclusions in alluvial diamonds in the northeastern Siberian Platform. *Russian Geology and Geophysics*, *52*, 1286–1297.

Luth, R. W. (2001). Experimental determination of the reaction aragonite+magnesite = dolomite at 5 to 9 GPa. *Contributions to Mineralogy and Petrology*, *141*, 222–232.

Luth, R. W. (2006). Experimental study of the $CaMgSi_2O_6–CO_2$ system at 3–8 GPa. *Contributions to Mineralogy and Petrology*, *151*, 141–157.

Maeda, F., E. Ohtani, S. Kamada, T. Sakamaki, N. Hirao, & Y. Ohishi (2017). Diamond formation in the deep lower mantle: a high-pressure reaction of $MgCO_3$ and SiO_2. *Scientific Reports*, *7*, 40602.

Mao, Z., M. Armentrout, E. Rainey, C. E. Manning, P. Dera, V. B. Prakapenka, & A. Kavner (2011). Dolomite III: A new candidate lower mantle carbonate. *Geophysical Research Letters*, *38*, L22303, doi: 22310.21029/22011GL049519.

Martinez, I., A. Deutsch, U. Schärer, P. Ildefonse, F. Guyot, & P. Agrinier (1995). Shock recovery experiments on dolomite and thermodynamical calculations of impact induced decarbonation. *Journal of Geophysical Research: Solid Earth*, *100*, 15465–15476.

Martinez, I., J. Z. Zhang, & R. J. Reeder (1996). In situ X-ray diffraction of aragonite and dolomite at high pressure and high temperature: Evidence for dolomite breakdown to aragonite and magnesite. *American Mineralogist*, *81*, 611–624.

Martirosyan, N. S., K. D. Litasov, S. S. Lobanov, A. F. Goncharov, A. Shatskiy, H. Ohfuji, & V. B. Prakapenka (2019). The Mg-carbonate–Fe interaction: Implication for the fate of subducted carbonates and formation of diamond in the lower mantle. *Geoscience Frontiers*, *10,* 1449–1458.

Martirosyan, N. S., T. Yoshino, A. Shatskiy, A. D. Chanyshev, & K. D. Litasov (2016). The $CaCO_3$–Fe interaction: Kinetic approach for carbonate subduction to the deep Earth's mantle. *Physics of the Earth and Planetary Interiors*, *259*, 1–9.

Mattila, A., T. Pylkkänen, J. Rueff, S. Huotari, G. Vanko, M. Hanfland, M. Lehtinen, et al. (2007). Pressure induced magnetic transition in siderite $FeCO_3$ studied by X-ray emission spectroscopy, *Journal of Physics: Condensed Matter*, *19*, 386206.

McKie, D. (1990). Subsolidus phase relations in the system $K_2Ca(CO_3)_2–Na_2Mg(CO_3)_2$ at 1 kbar; the fairchildite ss-buetschliite-eitelite eutectoid. *American Mineralogist*, *75*, 1147–1150.

Mellot-Draznieks, C., S. Girard, G. Ferey, J. C. Schon, Z. Cancarevic, & M. Jansen (2002). Computational design and prediction of interesting not-yet-synthesized structures of inorganic materials by using building unit concepts. *Chemistry-a European Journal*, *8*, 4103–4113.

Menzies, M., & C. Hawkesworth (1986). *Mantle metasomatism*, Academic Press, London.

Merlini, M., V. Cerantola, G. D. Gatta, M. Gemmi, M. Hanfland, I. Kupenko, P. Lotti, et al. (2017). Dolomite-IV: Candidate structure for a carbonate in the Earth's lower mantle. *American Mineralogist*, *102*, 1763–1766.

Merlini, M., W. A. Crichton, M. Hanfland, M. Gemmi, H. Müller, I. Kupenko, & L. Dubrovinsky (2012a). Structures of dolomite at ultrahigh pressure and their influence on the deep carbon cycle. *Proceedings of the National Academy of Sciences*, *109*, 13509–13514.

Merlini, M., M. Hanfland, & W. A. Crichton (2012b). $CaCO_3$-III and $CaCO_3$-VI, high-pressure polymorphs of calcite: Possible host structures for carbon in the Earth's mantle, *Earth and Planetary Science Letters*, *333–334*, 265–271.

Mirwald, P. W. (1976). A differential thermal analysis study of the high-temperature polymorphism of calcite at high pressure. *Contributions to Mineralogy and Petrology*, *59*, 33–40.

Mitchell, R. H., & B. A. Kjarsgaard (2011). Experimental studies of the system $Na_2CO_3–CaCO_3–MgF_2$ at 0.1 GPa: Implications for the differentiation and low-temperature crystallization of natrocarbonatite. *Journal of Petrology*, *52*, 1265–1280.

Molina, J. F., & S. Poli (2000). Carbonate stability and fluid composition in subducted oceanic crust: an experimental study on H_2O-CO_2-bearing basalts. *Earth and Planetary Science Letters*, *176*, 295–310.

Moore, K. R. (2012). Experimental study in the $Na_2O–CaO–MgO–Al_2O_3–SiO_2–CO_2$ system at 3 GPa: the effect of sodium

on mantle melting to carbonate-rich liquids and implications for the petrogenesis of silicocarbonatites. *Mineralogical Magazine*, *76*, 285–309.

Morlidge, M., A. Pawley, & G. Droop (2006). Double carbonate breakdown reactions at high pressures: an experimental study in the system CaO–MgO–FeO–MnO–CO_2. *Contributions to Mineralogy and Petrology*, *152*, 365–373.

Müller, J., M. Koch-Müller, D. Rhede, F. D. Wilke, & R. Wirth (2017). Melting relations in the system $CaCO_3$–$MgCO_3$ at 6 GPa. *American Mineralogist*, *102*, 2440–2449.

Navon, O., I. Hutcheon, G. Rossman, & G. Wasserburg (1988). Mantle-derived fluids in diamond micro-inclusions. *Nature*, *335*, 784–789.

Niggli, P. (1916). Gleichgewichte zwischen TiO_2 und CO_2, sowie SiO_2 und CO_2 in alkali-, kalk-alkali und alkali-aluminatschmelzen. *Zeitschrift Fur Anorganische Und Allgemeine Chemie*, *98*, 241–326.

Oganov, A. R., S. Ono, Y. M. Ma, C. W. Glass, & A. Garcia (2008). Novel high-pressure structures of $MgCO_3$, $CaCO_3$ and CO_2 and their role in Earth's lower mantle. *Earth and Planetary Science Letters*, *273*, 38–47.

Ono, S., T. Kikegawa, & Y. Ohishi (2007). High-pressure transition of $CaCO_3$. *American Mineralogist*, *92*, 1246–1249.

Ono, S., T. Kikegawa, Y. Ohishi, & J. Tsuchiya (2005). Post-aragonite phase transformation in $CaCO_3$ at 40 GPa. *American Mineralogist*, *90*, 667–671.

Pickard, C. J., & R. J. Needs (2015). Structures and stability of calcium and magnesium carbonates at mantle pressures. *Physical Review B*, *91*, 104101.

Pinto, L. G. R., M. B. de Pádua, N. Ussami, Í. Vitorello, A. L. Padilha, & C. Braitenberg (2010). Magnetotelluric deep soundings, gravity and geoid in the south São Francisco craton: Geophysical indicators of cratonic lithosphere rejuvenation and crustal underplating. *Earth and Planetary Science Letters*, *297*, 423–434.

Pippinger, T., R. Miletich, M. Merlini, P. Lotti, P. Schouwink, T. Yagi, W. A. Crichton, et al. (2015). Puzzling calcite-III dimorphism: crystallography, high-pressure behavior, and pathway of single-crystal transitions. *Physics and Chemistry of Minerals*, *42*, 29–43.

Plank, T., & C. H. Langmuir (1998). The chemical composition of subducting sediment and its consequences for the crust and mantle. *Chemical Geology*, *145*, 325–394.

Podborodnikov, I. V., A. Shatskiy, A. V. Arefiev, A. D. Chanyshev, & K. D. Litasov (2018). The system Na_2CO_3–$MgCO_3$ at 3 GPa. *High Pressure Research*, *38*, 281–292.

Podborodnikov, I. V., A. Shatskiy, A. V. Arefiev, & K. D. Litasov (2019). Phase relations in the system Na_2CO_3–$CaCO_3$–$MgCO_3$ at 3 GPa with implications for carbonatite genesis and evolution. *Lithos*, *330–331*, 74–89.

Podborodnikov, I. V., A. Shatskiy, A. V. Arefiev, S. V. Rashchenko, A. D. Chanyshev, & K. D. Litasov (2018). The system Na_2CO_3–$CaCO_3$ at 3 GPa. *Physics and Chemistry of Minerals*, *45*, 773–787.

Pokhilenko, N. P., A. M. Agashev, K. D. Litasov, & L. N. Pokhilenko (2015). Carbonatite metasomatism of peridotite lithospheric mantle: implications for diamond formation and carbonatite-kimberlite magmatism. *Russian Geology and Geophysics*, *56*, 280–295.

Ragone, S. E., R. K. Datta, D. M. Roy, & O. F. Tuttle (1966). The system potassium carbonate-magnesium carbonate. *Journal of Physical Chemistry*, *70*, 3360–3361.

Rainey, E. S. G., J. W. Hernlund, & A. Kavner (2013). Temperature distributions in the laser-heated diamond anvil cell from 3-D numerical modeling. *Journal of Applied Physics*, *114*, 204905.

Ratajeski, K., & T. W. Sisson (1999). Loss of iron to gold capsules in rock-melting experiments. *American Mineralogist*, *84*, 1521–1527.

Rosenberg, P. E. (1963). Subsolidus relations in the system $CaCO_3$–$FeCO_3$. *American Journal of Science*, *261*, 683–689.

Rudnick, R. L., W. F. McDonough, & B. W. Chappell (1993). Carbonatite metasomatism in the northern Tanzanian mantle: petrographic and geochemical characteristics. *Earth and Planetary Science Letters*, *114*, 463–475.

Salje, E., & K. Viswanathan (1976). The phase diagram calcite-aragonite as derived from the crystallographic properties. *Contributions to Mineralogy and Petrology*, *55*, 55–67.

Santillán, J., Q. Williams, & E. Knittle (2003). Dolomite-II: A high-pressure polymorph of $CaMg(CO_3)_2$. *Geophysical Research Letters*, *30*, 1054, doi: 1010.1029/2002GL016018

Sato, K., & T. Katsura (2001). Experimental investigation on dolomite dissociation into aragonite+magnesite up to 8.5 GPa. *Earth and Planetary Science Letters*, *184*, 529–534.

Schneide, S. J., & E. M. Levin (1973). Polymorphism of K_2CO_3. *Journal of the American Ceramic Society*, *56*, 218–219.

Sharygin, I., K. Litasov, A. Shatskiy, A. Golovin, E. Ohtani, & N. Pokhilenko (2015). Melting phase relations of the Udachnaya-East group-I kimberlite at 3.0–6.5 GPa: Experimental evidence for alkali-carbonatite composition of primary kimberlite melts and implications for mantle plumes. *Gondwana Research*, *28*, 1391–1414.

Sharygin, I. S., A. V. Golovin, A. V. Korsakov, & N. P. Pokhilenko (2013). Eitelite in sheared peridotite xenoliths from Udachnaya-East kimberlite pipe (Russia) – a new locality and host rock type. *European Journal of Mineralogy*, *25*, 825–834.

Shatskiy, A., Y. M. Borzdov, K. D. Litasov, I. N. Kupriyanov, E. Ohtani, & Y. N. Palyanov (2014). Phase relations in the system $FeCO_3$–$CaCO_3$ at 6 GPa and 900–1700 °C and its relation to the system $CaCO_3$–$FeCO_3$–$MgCO_3$. *American Mineralogist*, *99*, 773–785.

Shatskiy, A., Y. M. Borzdov, K. D. Litasov, I. S. Sharygin, Y. N. Palyanov, & E. Ohtani (2015). Phase relationships in the system K_2CO_3–$CaCO_3$ at 6 GPa and 900–1450°C. *American Mineralogist*, *100*, 223–232.

Shatskiy, A., P. N. Gavryushkin, I. S. Sharygin, K. D. Litasov, I. N. Kupriyanov, Y. Higo, Y. M. Borzdov, et al. (2013). Melting and subsolidus phase relations in the system Na_2CO_3–$MgCO_3$±H_2O at 6 GPa and the stability of $Na_2Mg(CO_3)_2$ in the upper mantle. *American Mineralogist*, *98*, 2172–2182.

Shatskiy, A., T. Katsura, K. D. Litasov, A. V. Shcherbakova, Y. M. Borzdov, D. Yamazaki, A. Yoneda, et al. (2011). High pressure generation using scaled-up Kawai-cell. *Physics of the Earth and Planetary Interiors*, *189*, 92–108.

Shatskiy, A., K. D. Litasov, E. Ohtani, Y. M. Borzdov, A. I. Khmelnicov, & Y. N. Palyanov (2015). Phase relations in the K_2CO_3–$FeCO_3$ and $MgCO_3$–$FeCO_3$ systems at 6 GPa and 900–1700 °C. *European Journal of Mineralogy*, *27*, 487–499.

Shatskiy, A. F., K. D. Litasov, & Y. N. Palyanov (2015). Phase relations in carbonate systems at pressures and temperatures of lithospheric mantle: Review of experimental data. *Russian Geology and Geophysics*, *56*, 113–142.

Shatskiy, A., K. D. Litasov, Y. N. Palyanov, & E. Ohtani (2016). Phase relations on the K_2CO_3–$CaCO_3$–$MgCO_3$ join at 6 GPa and 900–1400 °C: Implications for incipient melting in carbonated mantle domains. *American Mineralogist*, *101*, 437–447.

Shatskiy, A., K. D. Litasov, I. S. Sharygin, I. A. Egonin, A. M. Mironov, Y. N. Palyanov, & E. Ohtani (2016). The system Na_2CO_3–$CaCO_3$–$MgCO_3$ at 6 GPa and 900–1250 °C and its relation to the partial melting of carbonated mantle. *High Pressure Research*, *36*, 23–41.

Shatskiy, A., K. D. Litasov, I. S. Sharygin, & E. Ohtani (2017). Composition of primary kimberlite melt in a garnet lherzolite mantle source: constraints from melting phase relations in anhydrous Udachnaya-East kimberlite with variable CO_2 content at 6.5 GPa. *Gondwana Research*, *45*, 208–227.

Shatskiy, A., K. D. Litasov, H. Terasaki, T. Katsura, & E. Ohtani (2010). Performance of semi-sintered ceramics as pressure-transmitting media up to 30 GPa. *High Pressure Research*, *30*, 443–450.

Shatskiy, A., I. V. Podborodnikov, A. V. Arefiev, K. D. Litasov, A. D. Chanyshev, I. S. Sharygin, N. S. Karmanov, et al. (2017). Effect of alkalis on the reaction of clinopyroxene with Mg-carbonate at 6 GPa: Implications for partial melting of carbonated lherzolite. *American Mineralogist*, *102*, 1934–1946.

Shatskiy, A., I. V. Podborodnikov, A. V. Arefiev, D. A. Minin, A. D. Chanyshev, & K. D. Litasov (2018). Revision of the $CaCO_3$–$MgCO_3$ phase diagram at 3 and 6 GPa. *American Mineralogist*, *103*, 441–452.

Shatskiy, A., S. V. Rashchenko, E. Ohtani, K. D. Litasov, M. V. Khlestov, Y. M. Borzdov, I. N. Kupriyanov, et al. (2015). The system Na_2CO_3–$FeCO_3$ at 6 GPa and its relation to the system Na_2CO_3–$FeCO_3$–$MgCO_3$. *American Mineralogist*, *100*, 130–137.

Shatskiy, A., I. S. Sharygin, P. N. Gavryushkin, K. D. Litasov, Y. M. Borzdov, A. V. Shcherbakova, Y. Higo, et al. (2013). The system K_2CO_3–$MgCO_3$ at 6 GPa and 900–1450 °C. *American Mineralogist*, *98*, 1593–1603.

Shatskiy, A., I. S. Sharygin, K. D. Litasov, Y. M. Borzdov, Y. N. Palyanov, & E. Ohtani (2013). New experimental data on phase relations for the system Na_2CO_3–$CaCO_3$ at 6 GPa and 900–1400 °C. *American Mineralogist*, *98*, 2164–2171.

Shirasaka, M., E. Takahashi, Y. Nishihara, K. Matsukage, & T. Kikegawa (2002). In situ X-ray observation of the reaction dolomite = aragonite+magnesite at 900–1300 K. *American Mineralogist*, *87*, 922–930.

Shu, Q., & G. P. Brey (2015). Ancient mantle metasomatism recorded in subcalcic garnet xenocrysts: temporal links between mantle metasomatism, diamond growth and crustal tectonomagmatism. *Earth and Planetary Science Letters*, *418*, 27–39.

Smith, D., K. V. Lawler, M. Martinez-Canales, A. W. Daykin, Z. Fussell, G. A. Smith, C. Childs, et al. (2018). Postaragonite phases of $CaCO_3$ at lower mantle pressures. *Physical Review Materials*, *2*, 013605.

Sokolova, T. S., P. I. Dorogokupets, A. M. Dymshits, B. S. Danilov, & K. D. Litasov (2016). Microsoft excel spreadsheets for calculation of PVT relations and thermodynamic properties from equations of state of MgO, diamond and nine metals as pressure markers in high-pressure and high-temperature experiments. *Computers & Geosciences*, *94*, 162–169.

Sokolova, T. S., P. I. Dorogokupets, & K. D. Litasov (2013). Self-consistent pressure scales based on the equations of state for ruby, diamond, MgO, B2-NaCl, as well as Au, Pt and other metals to 4 Mbars and 3000 K. *Russian Geology and Geophysics*, *54*, 181–199.

Solomatova, N. V., & P. D. Asimow (2018). First-principles calculations of high-pressure iron-bearing monoclinic dolomite and single-cation carbonates with internally consistent Hubbard U. *Physics and Chemistry of Minerals*, *45*, 293–302.

Solopova, N. A., L. Dubrovinsky, A. V. Spivak, Y. A. Litvin, & N. Dubrovinskaia (2015). Melting and decomposition of $MgCO_3$ at pressures up to 84 GPa. *Physics and Chemistry of Minerals*, *42*, 73–81.

Spivak, A. V., Y. A. Litvin, S. V. Ovsyannikov, N. A. Dubrovinskaia, & L. S. Dubrovinsky (2012). Stability and breakdown of $Ca^{13}CO_3$ melt associated with formation of ^{13}C-diamond in static high pressure experiments up to 43 GPa and 3900 K. *Journal of Solid State Chemistry*, *191*, 102–106.

Stachel, T., J. W. Harris, & G. P. Brey (1998). Rare and unusual mineral inclusions in diamonds from Mwadui, Tanzania. *Contributions to Mineralogy and Petrology*, *132*, 34–47.

Stagno, V., D. O. Ojwang, C. A. McCammon, & D. J. Frost (2013). The oxidation state of the mantle and the extraction of carbon from Earth's interior. *Nature*, *493*, 84–88.

Stagno, V., V. Stopponi, Y. Kono, C. E. Manning, & T. Irifune (2018). Experimental determination of the viscosity of Na_2CO_3 melt between 1.7 and 4.6 GPa at 1200–1700°C: Implications for the rheology of carbonatite magmas in the Earth's upper mantle. *Chemical Geology*, *501*, 19–25.

Staudigel, H. (2014). Chemical fluxes from hydrothermal alteration of the oceanic crust, in Turekian, K. K., Holland, H. D (Eds.), *Treatise on Geochemistry* (2nd ed., pp. 583–606), Oxford: Elsevier.

Suito, K., J. Namba, T. Horikawa, Y. Taniguchi, N. Sakurai, M. Kobayashi, A. Onodera, et al. (2001). Phase relations of $CaCO_3$ at high pressure and high temperature. *American Mineralogist*, *86*, 997–1002.

Swainson, I. P., M. T. Dove, & M. J. Harris (1995). Neutron powder diffraction study of the ferroelastic phase transition and lattice melting in sodium carbonate, Na_2CO_3. *Journal of Physics-Condensed Matter*, *7*, 4395–4417.

Sweeney, R. J. (1994). Carbonatite melt compositions in the Earth's mantle. *Earth and Planetary Science Letters*, *128*, 259–270.

Sweeney, R. J., T. J. Falloon, & D. H. Green (1995). Experimental constraints on the possible mantle origin of natrocarbonatite. In Bell, K., Keller, J. (Eds.), *Carbonatite Volcanism* (pp. 191–207), Springer.

Tao, R., Y. Fei, & L. Zhang (2013). Experimental determination of siderite stability at high pressure. *American Mineralogist*, *98*, 1565–1572.

Tao, R., L. Zhang, Y. Fei, & Q. Liu (2014). The effect of Fe on the stability of dolomite at high pressure: Experimental study and petrological observation in eclogite from southwestern Tianshan, China. *Geochimica et Cosmochimica Acta*, *143*, 253–267.

Thibault, Y., A. D. Edgar, & F. E. Lloyd (1992). Experimental investigation of melts from a carbonated phlogopite lherzolite: implications for metasomatism in the continental lithospheric mantle. *American Mineralogist*, *77*, 784–794.

Thomson, A. R., M. J. Walter, S. C. Kohn, & R. A. Brooker (2016). Slab melting as a barrier to deep carbon subduction. *Nature*, *529*, 76–79.

Tsuno, K., R. Dasgupta, L. Danielson, & K. Righter (2012). Flux of carbonate melt from deeply subducted pelitic sediments: Geophysical and geochemical implications for the source of Central American volcanic arc. *Geophysical Research Letters*, *39*, L16307, doi:10.1029/2012gl052606.

Wallace, M. E., & D. H. Green (1988). An experimental determination of primary carbonatite magma composition. *Nature*, *335*, 343–346.

Wang, M., Q. Liu, T. Inoue, B. Li, S. Pottish, J. Wood, C. Yang, et al. (2016). The K_2CO_3 fusion curve revisited: New experiments at pressures up to 12 GPa. *Journal of Mineralogical and Petrological Sciences*, *111*, 241–251.

Weidner, J. R. (1972). Equilibria in the system Fe–CO; Part I, Siderite-magnetite-carbon-vapor equilibrium from 500 to 10,000 bars. *American Journal of Science*, *272*, 735–751.

Weidner, J. R. (1982). Iron-oxide magmas in the system Fe–CO. *Canadian Mineralogist*, *20*, 555–566.

Weiss, Y., R. Kessel, W. L. Griffin, I. Kiflawi, O. Klein-BenDavid, D. R. Bell, J. W. Harris, et al. (2009). A new model for the evolution of diamond-forming fluids: Evidence from microinclusion-bearing diamonds from Kankan, Guinea. *Lithos*, *112*(S2). 660–674.

Wyllie, P. J., & W. L. Huang (1975). Inflence of mantle CO_2 ingeneration of carbonatites and kimberlites. *Nature*, *257*, 297–299.

Wyllie, P. J., & W. L. Huang (1976). Carbonation and melting reactions in the system $CaO–MgO–SiO_2–CO_2$ at mantle pressures with geophysical and petrological applications. *Contributions to Mineralogy and Petrology*, *54*, 79–107.

Yaxley, G. M., & G. P. Brey (2004). Phase relations of carbonate-bearing eclogite assemblages from 2.5 to 5.5 GPa: implications for petrogenesis of carbonatites. *Contributions to Mineralogy and Petrology*, *146*, 606–619.

Yaxley, G. M., A. J. Crawford, & D. H. Green (1991). Evidence for carbonatite metasomatism in spinel peridotite xenoliths from western Victoria, Australia. *Earth and Planetary Science Letters*, *107*, 305–317.

Yaxley, G. M., & D. H. Green (1994). Experimental demonstration of refractory carbonate-bearing eclogite and siliceous melt in the subduction regime. *Earth and Planetary Science Letters*, *128*, 313–325.

Yaxley, G. M., & D. H. Green (1996). Experimental reconstruction of sodic dolomitic carbonatite melts from metasomatised lithosphere. *Contributions to Mineralogy and Petrology*, *124*, 359–369.

Yaxley, G. M., D. H. Green, & V. Kamenetsky (1998). Carbonatite metasomatism in the southeastern Australian lithosphere. *Journal of Petrology*, *39*, 1917–1930.

Yoshino, T., B. Gruber, & C. Reinier (2018). Effects of pressure and water on electrical conductivity of carbonate melt with implications for conductivity anomaly in continental mantle lithosphere. *Physics of the Earth and Planetary Interiors*, *281*, 8–16.

Zaitsev, A. N., & J. Keller (2006). Mineralogical and chemical transformation of Oldoinyo Lengai natrocarbonatites, Tanzania. *Lithos*, *91*, 191–207.

Zedgenizov, D. A., A. L. Ragozin, V. S. Shatsky, D. Araujo, & W. L. Griffin (2011). Fibrous diamonds from the placers of the northeastern Siberian Platform: carbonate and silicate crystallization media. *Russian Geology and Geophysics*, *52*, 1298–1309.

Zedgenizov, D. A., S. Rege, W. L. Griffin, H. Kagi, & V. S. Shatsky (2007). Composition of trapped fluids in cuboid fibrous diamonds from the Udachnaya kimberlite: LAM-ICPMS analysis. *Chemical Geology*, *240*, 151–162.

Zedgenizov, D. A., A. Shatskiy, A. L. Ragozin, H. Kagi, & V. S. Shatsky (2014). Merwinite in diamond from São Luiz, Brazil: A new mineral of the Ca-rich mantle environment. *American Mineralogist*, *99*, 547–550.

Zhang, Z., Z. Mao, X. Liu, Y. Zhang, & J. Brodholt (2018). Stability and reactions of $CaCO_3$ polymorphs in the Earth's deep mantle. *Journal of Geophysical Research: Solid Earth*, *123*, 6491–6500.